



## Effect of dynamic contact angle in a volume of fluid (VOF) model for a microfluidic capillary flow

Auro Ashish Saha<sup>a</sup>, Sushanta K. Mitra<sup>b,\*</sup>

<sup>a</sup>Department of Mechanical Engineering, Indian Institute of Technology Bombay, Mumbai, India

<sup>b</sup>Department of Mechanical Engineering, University of Alberta, Canada

### ARTICLE INFO

#### Article history:

Received 4 June 2009

Accepted 31 July 2009

Available online 9 August 2009

#### Keywords:

Capillary flow

Dynamic contact angle

Microchannels

Pillars

### ABSTRACT

We perform three-dimensional numerical and experimental study of the dynamic contact angle using volume of fluid (VOF) method applied to microfluidic channels with integrated pillars. Initially, we evaluated different dynamic contact angle models (hydrodynamic, molecular kinetic and empirical) for capillary filling of a two-dimensional microchannel using analytical formulation. Further, the models which require a minimum prescription of adjustable parameters are only used for the study of capillary filling of microchannels with integrated pillars using different working fluids such as DI water, ethanol and isopropyl alcohol. Different microchannel geometry with varying diameter/height/spacing were studied for circular pillars. Effect of square pillars and changing the overall number of pillars on the capillary phenomena were also simulated. Our study demonstrated that the dynamic contact angle models modifies the transient response of the meniscus displacement and also the observed trends are model specific for the various microchannel geometries and working fluids. However, the different models have minimal effect on the meniscus profile. Different inlet boundary conditions were applied to observe the effect of grid resolution selected for numerical study on the capillary filling time. A grid dependent dynamic contact angle model which incorporates effective slip in the model was also used to observe the grid convergence of the numerical results. The grid independence was shown to improve marginally by applying the grid dependent dynamic contact angle model. Further we did numerical experiments of capillary filling considering variable surface wettability on the top and bottom walls of the microchannel with alternate hydrophilic–hydrophobic patterns. The meniscus front pinning was noticed for a high wetting contrast between the patterns. Non uniform streamline patterns indicated mixing of the fluid when using patterned walls. Such a microfluidic device with variable surface properties with integrated pillars may be useful for carrying out biological operations that often require effective separation and mixing of the fluids.

© 2009 Elsevier Inc. All rights reserved.

### 1. Introduction

Flow control is essential in many of the microfluidic systems targeted for use in biochemistry analysis, drug delivery, and sequencing or synthesis of nucleic acids, among others. Such systems use microchannels to promote efficient mixing without the use of any external means. Capillary flow, which is purely governed by the surface tension forces, is predominantly used for the transport of the fluid into microfluidic devices. Pillar structures are often used in microchannels to increase the surface/volume ratio and increase the capillary flow. Such devices often have complex geometries, like pillar structures [1], for which analytical solution to obtain the fluid distribution (meniscus front shapes) is often difficult. The front shapes, which is a measure of, how well the fluid

gets distributed, is an important parameter to ensure reliability and performance of microfluidic devices. Hence it becomes necessary to rely on numerical techniques to predict the flow phenomena in such cases.

Research on patterned surfaces reveal interesting phenomena that can be exploited to control liquid motions in microfluidic devices. It is possible to exploit the chemical or geometrical patterning of a surface to control the flow within the microchannels. Huang et al. [2] have studied theoretically and numerically the capillary filling flows inside patterned surface microchannels. Two different patterned microchannel configurations – inner walls patterned with unequal contact angles; each inner wall divided into two equal segments having different contact angles have been considered for carrying out two-dimensional and three-dimensional simulations. An equivalent contact angle model based on the surface energy method has been proposed for estimating capillary flows inside the patterned surface

\* Corresponding author.

E-mail address: [sushanta.mittra@ualberta.ca](mailto:sushanta.mittra@ualberta.ca) (S.K. Mitra).

microchannels and they validated the model with traditional capillary rise theories. Saha and Mitra [3,4] have studied numerically the free surface flow inside patterned surface microchannels with alternate layers of different sizes of hydrophilic and hydrophobic surfaces at the bottom wall. The pattern size and the surface tension of the fluid are found to have significant influence on the capillary phenomena in the patterned microchannel. Such patterned microchannel can be utilized to manipulate and optimize fluid flow in microfluidic devices. Such patterned configurations has so far been applied only to simple microchannel geometries.

Over the last few years, attempts have been made by number of researchers to simulate such passive transport in microchannels. The volume of fluid (VOF) technique [5], is the most commonly used technique for the simulation of free surfaces within commercial and academic CFD packages. The VOF model includes the effects of surface tension along the interface between each pair of phases. The model can be augmented by the additional specification of the contact angles between the phases and the walls [6].

The theoretical studies on wetting carried out in the last decades have led to a number of theoretical dynamic contact angle models. In all of these models the dynamic contact angle is expressed as function of contact line speed. There are about eight models on dynamic contact angles, namely Blake, Bracke, Cox, Jiang, Kalliadasis, Kistler, Newman and Shikhmurzaev that are based on hydrodynamic, molecular kinetic and empirical models [7,8]. The models are used mainly for capillary geometry such as meniscus rise in a vertical/horizontal tube, plate withdrawal, droplet impact, droplet spreading, coating etc. The dynamic contact angle relations are applied to analytical solution of the above capillary flow problems. Other techniques often used also include molecular dynamics, dissipative particle dynamics, LBM, FEM and CFD. Most of the models need adjustable parameter to match the experimental data on dynamic contact angle. Not all the dynamic contact angle models can be applied for the entire range of contact angles and other operating parameters [9]. It is necessary that, a dynamic contact angle model incorporates all the effects that influence the capillary phenomena in the microfluidic systems. Otherwise, with a free choice of the relevant adjustable parameters, it may result in inappropriate application of dynamic contact angle models [10].

Hirt and Brethour [11] mention that in VOF algorithm approach, dynamic contact angles are not specified but computed as part of the solution via the finite volume method (FVM). They arise automatically from the basic balance of forces on which the numerical method is built. This is one of the several practical advantages of this modeling approach. VOF algorithm calculates only the macroscopic effects of surface tension, and it tracks the interface progression under this force; it does not impose the specified contact angle to the interface at the wall. This is a macroscopic representation of the effects occurring due to nanoscale interactions between the two fluids and the surface, yet it is found to mimic observed phenomena quite well [12].

Dynamic systems involving a three-phase contact line are usually divided into two distinct categories [13], those in which the advancing (or receding) interface is driven with a constant velocity relative to the solid substrate, also called forced, or, steady displacement wetting; and those in which the interface is in nonequilibrium state, relaxing to a configuration of minimum free energy. The later is a nonsteady process, where the triple line velocity is a decreasing function of time. Most microfluidic studies are not concerned with the dependence of contact angle on the contact line speed [14], as it will have less pronounced effect due to extremely low fluid velocity encountered in the devices.

Other noteworthy fact which remains unaddressed is the use of the dynamic contact angle theory in three-dimensional complex microfluidic geometry. These are the very issues that this present paper aims to address, i.e., influence of dynamic contact angle theories on capillary flow in a microchannel with integrated pillars. The particular microchannel under investigation has complex three-dimensional geometry consisting of straight section, diverging section and section with arrays of integrated pillars in the present study. In the present study, passive capillary motion of fluid is simulated and a zero pressure gradient boundary condition is imposed at the microchannel inlet/outlet. Also, no-slip boundary conditions are imposed at the walls. However, this does not mean that the contact line with the wall cannot move, as the FVM code integrates over the whole cell adjacent to the wall to compute the mass flux of the dense phase, which, when using a finite grid size, will average out to give an apparent finite interface velocity at the wall [12]. Moreover, Renardy et al. [15] have showed that the contact line motion is not very sensitive (<5%) to the addition of artificial slip lengths with magnitudes in the order of the grid size.

CFD results often exhibit a mesh dependent results as reported in literature [16,3,17]. With the introduction of a macroscopic slip range in combination with a localized body force close to the contact line this turns out to be the remedy for this problem [16] of capillary filling in a microchannel. Afkhami et al. [17] have considered a mesh dependent dynamic contact angle model and showed mesh independent results for a plate withdrawal and drop spreading cases. Nevertheless, it is shown that the solution of the fluid dynamics problems involving contact angles dynamics are obtained on coarse meshes itself.

Our main objectives of the present study are as follows: (1) To apply the dynamic contact angle models for the capillary flow in microchannel with integrated pillars. (2) To consider different inlet boundary conditions to observe the effect of grid resolution and applying a grid dependent dynamic contact angle model with effective slip. (3) To study the capillary phenomena considering variable surface wettability on the top and bottom walls with alternate hydrophilic-hydrophobic patterns in the pillared microchannel.

The different parameters that we account in this study are geometric, such as length of the microchannel, diameter of the pillar, height of the microchannel, pitch of the pillars and volume of the microchannel; fluid physical properties, such as fluid surface tension and viscosity; flow variables, such as flow time, velocity and pressure; surface property, in the form of contact angle. It is often considered convenient to analyse results when expressed in a non-dimensional form when conducting parametric simulation. We have considered only two non-dimensional variables such as liquid volume fraction ( $F$ ) which is defined as the ratio of volume of fluid filled in the microchannel to the total volume and Capillary number (Ca) which is the ratio of viscous force to surface tension force. The fluids under consideration are DI water, ethanol and isopropyl as liquid and air as gas.

We have avoided considering non-dimensional parameters that involve ratios of viscosity, surface tension and density. At times the arbitrary choice of non-dimensional values of viscosity, surface tension and density ratio may represent unphysical fluid and often may not mimic existing real fluid behavior. In this study we specify a finite known pressure of  $0 \text{ N/m}^2$  at the inlet and outlet of the microchannel, so the choice of pressure variable in a non-dimensional parameter will not be appropriate here. Dynamic contact angle being a complex function of equilibrium contact angle and interface velocity is also not considered to form a non-dimensional parameter in this study.

## 2. Numerical simulation

### 2.1. Geometry of microchannel

The geometry of the microchannel model is shown in Fig. 1. The channel considered here is a three-dimensional channel with array of circular pillars of 350  $\mu\text{m}$  cross-section. The substrate materials for the microchannel under consideration are Polydimethylsiloxane (PDMS) and SU8. The pillars made of SU8/PDMS are arranged in line and separated by a distance of 300  $\mu\text{m}$ . The pillar height is 120  $\mu\text{m}$  for SU8 and 40  $\mu\text{m}$  for PDMS microchannel, respectively. This geometry of the channel is similar to that used by Saha and Mitra [1].

### 2.2. Governing equations

Equations for numerical (VOF model), analytical (reduced order model) solution and dynamic contact angle models for the propagation of a liquid in a channel is presented in the following sections.

#### 2.2.1. VOF model

The transient, three-dimensional numerical simulations of the capillary flow in the microchannel with integrated pillars are performed using VOF method [5]. The system consists of two incompressible and immiscible fluids represented as liquid and gas phases. Surface tension effects are incorporated in the VOF method. In this method we solve momentum equation and continuity equation. The flow is considered to be laminar, incompressible, Newtonian and isothermal with velocity field  $\mathbf{V}$  governed by the Navier-Stokes and continuity equations, which can be written as:

$$\nabla \cdot \mathbf{V} = 0 \quad (1)$$

$$\frac{\partial \rho \mathbf{V}}{\partial t} + \nabla \cdot (\rho \mathbf{V} \mathbf{V}) = -\nabla P + \rho \mathbf{g} + \nabla \cdot (\mu (\nabla \mathbf{V} + \nabla^T \mathbf{V})) + \mathbf{F}_s \quad (2)$$

where  $\mathbf{V}$  is the velocity of the mixture,  $P$  the pressure,  $t$  the time,  $\mathbf{F}_s$  the volumetric force at the interface resulting from surface tension, and  $\rho, \mu$  are the density and dynamic viscosity, respectively. In Eq. (2) the accumulation and convective momentum terms in every control volume (cell) balance the pressure force, gravity force, shear force, and additional surface tension force  $\mathbf{F}_s$ .

The physical properties of each fluid are calculated as weighted averages based on the volume fraction of the individual fluid in a

single cell. The fluid volume in a cell is computed as  $F_{vol} = FV_{cell}$ , where  $V_{cell}$  is the volume of a computational cell and  $F$  is the liquid volume fraction in a cell. The value of  $F$  in a cell should range between 1 and 0. Here,  $F = 1$  represents a cell which is completely filled with liquid,  $F = 0$  represents a cell which is completely filled with gas and  $0 < F < 1$  represents the liquid/gas interface.

The liquid volume fraction distribution can be determined by solving a separate passive transport equation, given as:

$$\frac{\partial F}{\partial t} + \mathbf{V} \cdot \nabla F = 0 \quad (3)$$

where,

$$F = \frac{\text{cell volume occupied by liquid}}{\text{total volume of the control cell}} \quad (4)$$

The mixture's physical properties are derived from that of the two phases through the volume fraction function. In particular, the average value of  $\rho$  and  $\mu$  in a computational cell can be computed from the value of  $F$  in accordance with:

$$\rho = F\rho_2 + (1 - F)\rho_1 \quad (5)$$

$$\mu = F\mu_2 + (1 - F)\mu_1 \quad (6)$$

where the subscripts 1 and 2 represent the gas and the liquid phases, respectively.

The surface tension model follows the continuum surface force (CSF) model proposed by Brackbill et al. [18]. The surface tension in Eq. (2) according to the CSF model is computed as:

$$\mathbf{F}_s = \sigma \kappa \nabla F \quad (7)$$

The surface tension is taken to be constant along the surface and only the forces normal to the interface are considered. According to the CSF model, the surface curvature  $\kappa$  is computed from local gradients in the surface normal to the interface, which is given as:

$$\kappa = \frac{1}{|\mathbf{n}|} \left( \left( \frac{\mathbf{n}}{|\mathbf{n}|} \cdot \nabla \right) |\mathbf{n}| - \nabla \cdot \mathbf{n} \right) \quad (8)$$

where  $\mathbf{n} = \nabla F$  is the normal vector. Wall adhesion is included in the model through the contact angle:

$$\hat{\mathbf{n}} = \hat{\mathbf{n}}_w \cos \theta + \hat{\mathbf{t}}_w \sin \theta \quad (9)$$

where  $\hat{\mathbf{n}}$  is the unit vector normal to the surface,  $\hat{\mathbf{n}} = \frac{\mathbf{n}}{|\mathbf{n}|}$ ,  $\hat{\mathbf{n}}_w$  and  $\hat{\mathbf{t}}_w$  represents the unit vector normal and tangent to the wall, respectively.

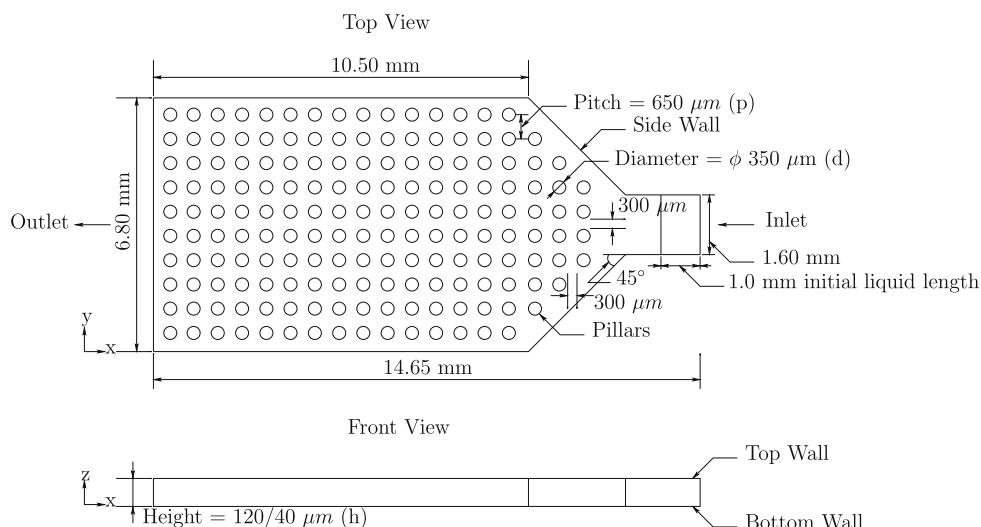


Fig. 1. Geometry of the microchannel.

Eqs. (1)–(9) are solved iteratively to obtain the liquid volume fraction and the velocity field solution under appropriate initial and boundary conditions. No slip boundary conditions at the walls are imposed. The current VOF methodology includes implicit/effective slip length at no-slip boundaries and the cell face normal velocities are utilized to advect volume fractions [17]. As an initial condition a distribution of  $F$  in the microchannel needs to be specified. The effect of gravity is not taken into account in the present study, as the Bond number ( $Bo$ ),  $\rho gh^2/\sigma$  is much less than unity, where  $h$  is the height of the microchannel,  $g$  is the acceleration due to gravity,  $\rho$  and  $\sigma$  are the fluid density and surface tension coefficient, respectively.

### 2.2. Reduced order model

The analytical solution is based on a reduced order model [19] and is derived here for clarity. A reduced order model [19] which accounts for inertial forces is considered for validating the numerical results with analytical solution for a rectangular micro-channel. The momentum conservation in a two-dimensional microchannel can be expressed in terms of a balance between the surface tension force, pressure overhead and wall viscous force. At time  $t$ , if  $L$  is the distance travelled by the liquid meniscus and  $u_{avg}$  is the average fluid velocity, then the momentum balance can be written as,

$$\frac{d}{dt}(\rho h L u_{avg}) = 2\sigma \cos \theta + \Delta Ph - \frac{12\mu L}{h} u_{avg} \quad (10)$$

For a passive capillary filling process,  $\Delta P = 0$ . Noting  $u_{avg} = dL/dt$ , Eq. (10) can be re-written as

$$\frac{d^2}{dt^2} L^2 + B \frac{d}{dt} L^2 = A \quad (11)$$

where,

$$A = \frac{4\sigma \cos \theta + 2\Delta Ph}{\rho h}, \quad B = \frac{12\mu}{\rho h^2}$$

Considering the initial liquid meniscus position in the channel as  $L_0$  and with zero velocity, the transient solution of the capillary filling problem is given as:

$$L = \left( \frac{A}{B^2} \exp(-Bt) + \frac{At}{B} + \left( L_0^2 - \frac{A}{B^2} \right) \right)^{\frac{1}{2}} \quad (12)$$

$$u_{avg} = \frac{A(1 - \exp(-Bt))}{2BL} \quad (13)$$

### 2.2.3. Dynamic contact angle models

In our numerical simulations we have applied different dynamic contact angle models. To describe the models, let  $\theta_d$  denote the dynamic contact angle, and  $\theta_e$  is (static) equilibrium value. The relation between the dynamic contact angle and contact line velocity for the models is discussed here,

The dependence of the dynamic contact angle on the velocity is suggested empirically by Jiang et al. [20], and is given by

$$\cos \theta_d = \cos \theta_e - (1 + \cos \theta_e) \tanh(4.96 \text{Ca}^{0.702}) \quad (14)$$

The dependence of the dynamic contact angle on the velocity is suggested by Shikhmurzaev [21], and is given as

$$\cos \theta_d = \cos \theta_e - \frac{2u(a_1 + a_2 u_0)}{(1 - a_2)[(a_1 + u^2)^{1/2} + u]} \quad (15)$$

where

$$u = a_3 \frac{\mu v}{\sigma}, \quad u_0 = \frac{\sin \theta_d - \theta_d \cos \theta_d}{\sin \theta_d \cos \theta_d - \theta_d}, \\ a_1 = 1 + (1 - a_2)(\cos \theta_e - a_4)$$

and  $a_2, a_3$  and  $a_4$  are some phenomenological constants (0.54, 12.5 and 0.07) [8].

Kalliadasis proposed a dynamic contact angle model [22] as:

$$|\tan \theta_d| = 7.48 \text{Ca}^{1/3} - 3.28 \lambda^{0.04} \text{Ca}^{0.293} \quad (16)$$

where  $\lambda = 10^{-8}$  [23].

The dynamic contact angle model proposed by Kistler [24] is as follows:

$$\cos \theta_d = 1 - 2 \tanh \left( 5.16 \left[ \frac{\text{Ca} + \text{fHI}}{1 + 1.31(\text{Ca} + \text{fHI})^{0.99}} \right]^{0.706} \right) \quad (17)$$

$$\text{fHI}^{0.706} = \frac{1}{5.16} \left[ 1 + 1.31 \text{fHI}^{0.99} \right]^{0.706} \tanh^{-1} \left[ \frac{1 - \cos \theta_e}{2} \right]$$

whereas the one proposed by Bracke [25] can be written as:

$$\cos \theta_d = \cos \theta_e - 2(1 + \cos \theta_e) \text{Ca}^{0.5} \quad (18)$$

The molecular kinetic theory of the moving contact line proposed by Blake [9] considers the energy dissipation at the triple line to occur through effective free-energy barriers for the displacement away or towards the three phase contact line of the fluid molecules. The dependence of the dynamic contact angle on the velocity  $v$  is given by

$$\cos \theta_d = \cos \theta_e - \frac{\sigma_0}{\sigma} \sinh^{-1} \frac{v}{v_0} \quad (19)$$

where  $\sigma_0$  is proportional to the thermal energy and has units of surface tension and  $v_0$  is a velocity determined by some molecular quantities such as average frequency of displacement and distance between minima of the effective free-energy [8].

The dependence of the dynamic contact angle on the velocity suggested by Cox [26], is given by

$$\theta_d^3 = \theta_e^3 + 144 \text{Ca} \quad (20)$$

The dependence of the dynamic contact angle on the velocity suggested by Newman [27], is given by

$$\cos \theta_d = \cos \theta_e (1 - e^{-\sigma t / \mu M}) \quad (21)$$

where  $M$  [28] is a constant which depends on the surface condition in contact with the fluid,  $\text{Ca} = \frac{\mu v}{\sigma}$ ,  $\theta_e$  = static contact angle,  $\theta_d$  = dynamic contact angle.

Now we intend to use Eqs. (14)–(21) in our VOF formulation and test their effectiveness in relation to the capillary filling process in a microfluidic system.

### 2.3. Initial and boundary conditions

Initially, at time  $t = 0$ , the liquid meniscus position in the channel is set as 1.00 mm from the inlet. No slip boundary condition is imposed on all the walls and the boundary conditions for the surface affinity are described by the contact angles. Passive capillary filling process is considered by specifying a constant pressure (atmospheric) at channel inlet and outlet. A liquid volume fraction value of unity and zero is specified at channel inlet and outlet, respectively.

### 2.4. Solution technique

Open source based CFD analysis code OpenFOAM 1.5 (Open Field Operation and Manipulation) which is written by OpenCFD Ltd. is used for the simulations here. The solution technique follows the finite volume numerics to solve systems of partial differential equations ascribed on any 3D unstructured mesh of polyhedral cells [29]. The solver implements the VOF two-phase algorithm for the computations which enables the capturing of

**Table 1**

Fluid properties at 20 °C used in simulation.

Physical property	DI water	Ethanol	Isopropyl alcohol	Air
Density (kg/m <sup>3</sup> )	1000	791	785	1.2019
Viscosity (mPa s)	1.0	1.2	2.43	0.0185
Surface tension (N/m)	0.0725	0.0214	0.0228	–

sharp fluid/fluid interfaces [30,31]. As a transient solution is desired for the present capillary driven flow, the selection of the time step has to be based such that the stability of the numerical simulation is ensured. Therefore, a target Courant–Friedrich’s–Lewy ( $CFL = |v|\delta t/h$ , where  $v$  is the interface velocity,  $h$  is the local cell dimension and  $t$  is time) number of 0.1 is applied for numerical stability of the simulation. This would allow the interface to cross 10% of the width of a grid cell during each time step in a VOF computation. PISO (Pressure Implicit with Splitting of Operators)

algorithm is adopted for pressure–velocity coupling and pressure correction. The necessary compression of the interface is achieved by introducing an additional artificial compression term into the VOF equation ( $\nabla \cdot (F(1 - F)V_r)$ , where  $V_r$  is a velocity field suitable to compress the interface. This artificial term is active only in the interface region due to the term  $F(1 - F)$ . It also helps in keeping the interface without getting separated, particularly for diverging flows. Initial time step of 1.0E–09 s is selected and the time step is allowed to automatically adjust based on the CFL number and interface velocity which ensures the stability in the solver. A convergence criteria of 0.0001 is specified to control the iterative solution process. In the numerical simulation, the symmetry boundary condition about the center plane is used because of the symmetric flow along the width and thickness of the microchannel, and thus quarter of the geometry is only computed. The isocontour of  $F = 0.5$  is usually applied to identify the interfacial position for computation and visualization purposes. The computations are

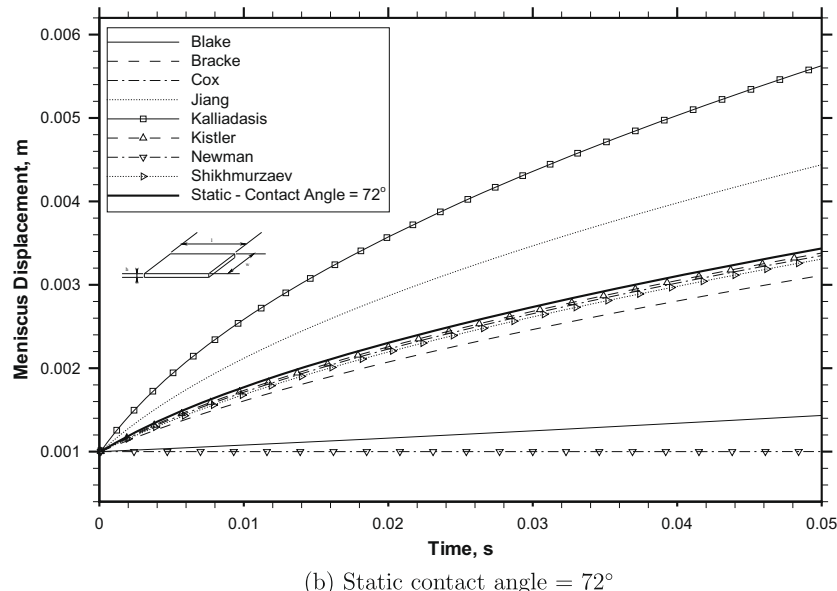
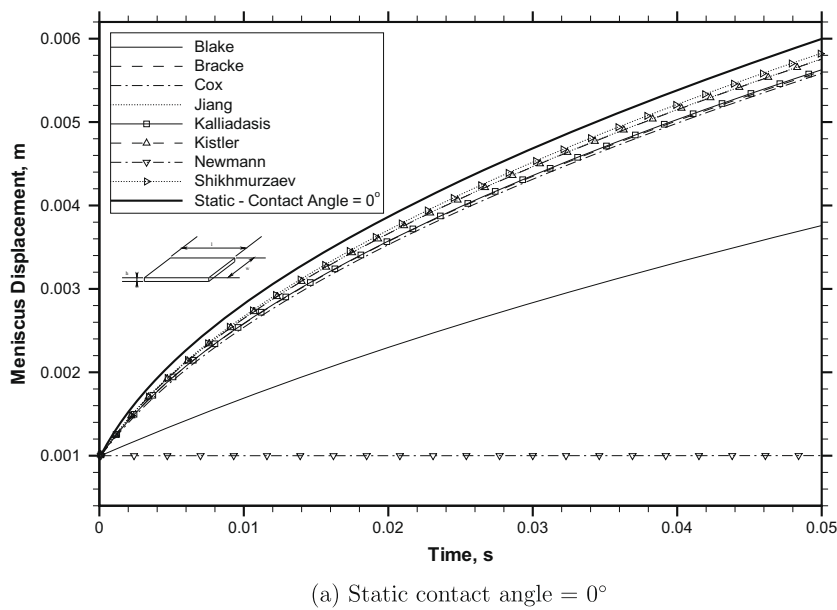


**Fig. 2.** Comparison of the position of the capillary meniscus with time obtained analytically for different dynamic contact angle models. The microchannel dimensions are – 40 μm height ( $h$ ), 7000 μm length ( $l$ ) and 3000 μm wide ( $w$ ).

performed both serially or parallelly within different clustered parallel environment available for computations. Parallel computations are based on open message passing interface (OpenMPI) or local area multicomputer message passing interface (LAM-MPI) library. The mesh has been decomposed using automatic load-balanced decomposition method (Metis) for parallel computations. The physical properties of DI water, ethanol and isopropyl alcohol used for simulations are provided in Table 1.

### 3. Results and discussion

#### 3.1. Effect of dynamic contact angle on the capillary flow

##### 3.1.1. Validation of dynamic contact angle models

Initially, we apply the different dynamic contact angle models to an analytical solution that is based on reduced order model [19] for capillary filling in a two-dimensional microchannel. The reduced order model is a transient solution which is derived accounting for the momentum change in the Navier–Stokes equation, obtained by averaging the Navier–Stokes equations across the liquid length in the microchannel. Fig. 2a and b shows the comparison of meniscus displacement obtained analytically based on the reduced order model [19] for different dynamic contact angle models for a fluid flow in a rectangular microchannel 40 μm in height, 7000 μm length and 3000 μm wide with black ink as working fluid ( $\rho = 1032.2 \text{ kg/m}^3$ ,  $\sigma = 0.072 \text{ N/m}$  and  $\mu = 0.00137 \text{ Pa s}$ ). The static contact angle for all models is kept at  $\theta_e = 0^\circ$  and  $\theta_d = 72^\circ$ . All the parameters required in the models are obtained from existing literature [28,8,22,25]. It is observed that the dynamic contact angle models modify the meniscus displacement with time, and the observed trend is model specific. We also find that the models of Kalliadasis and Jiang overpredicts the meniscus displacement when compared with static meniscus displacement, which indicates that these models are not suitable for partial wetting conditions, i.e., when the contact angle is greater than  $0^\circ$  as shown in Fig. 2b. The models of Blake and Newman show a very low value of meniscus displacement for the parameters selected here. Adjusting the parameters may result in predicting the meniscus displacement similar to other dynamic contact angle models. The models of Cox, Kistler and Shikhmurzaev show almost identical trend. The empirical model of Bracke predicts lower meniscus displacement compared to the other three models discussed earlier.

Based on the above analysis, we use Kistler, Kalliadasis and Bracke models and study the dynamic contact angle behavior on the free surface VOF algorithm [29].

Good agreement between numerical and analytical results is observed with the current VOF model formulation with dynamic contact angle models. Fig. 3 shows the comparison of meniscus displacement obtained numerically using VOF algorithm for different contact angle models with a reference case of static contact angle  $\theta_e = 36^\circ$  and  $0^\circ$ . It is observed that Kalliadasis's dynamic contact angle model is independent of the specified static contact angle as it depends only on the capillary number. It is again found that the applicability of such a model is only valid when the static contact angle is close to zero, i.e., for fully wet surfaces. However, the models based on Kistler and Bracke take into account the specified static contact angle and their applicability is valid for partially wet surfaces as well. The right bottom inset plot shows the variation of  $\cos \theta_d$  with the Capillary number  $Ca$ .

##### 3.1.2. Interaction of microchannel walls with the fluid

As the microchannel under study has a complicated geometry, it is important to understand how the surface adhesion force on the walls interact with the fluid. It must also be noted that a contact angle boundary condition specified on the walls will play a major role in the formation of the meniscus interface. The surface adhesion force acting on the top and bottom walls, side walls and the pillars will interact with the fluid. We observe that the contribution of the side walls is least among the three (1–3%), next is the contribution of pillars which may alter with the size of the pillar (5–13%) and finally the maximum contribution is from the top and bottom walls (85–95%) based on wettable area.

Fig. 4 shows the relative contribution of each of the microchannel walls on liquid volume fraction for static contact angle wall boundary condition. Here the working fluid is ethanol and the height of the pillared microchannel chosen for this study is 40 μm. The contact angle at a given wall is independently fixed at  $30^\circ$  where as the remaining walls are maintained at fully wet condition ( $0^\circ$ ). To save computational time, simulations are carried out for the channel length of 9450 μm for all the cases considered in this study. The liquid volume fraction variation is also plotted when static contact angles of  $30^\circ$  and  $0^\circ$  are applied on all the walls. It is observed that the top and bottom wall surface adhesions dominate compared to the side walls and pillars.

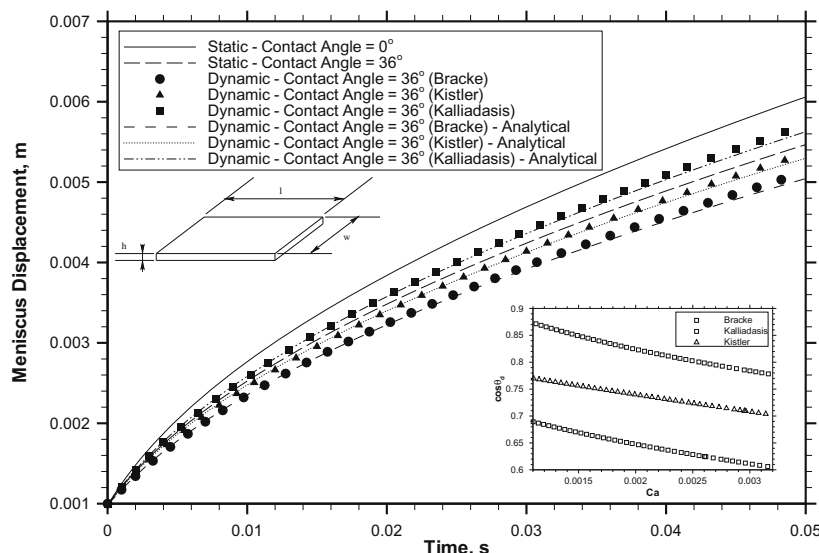


**Fig. 3.** Comparison of the position of the capillary meniscus with time obtained numerically for different dynamic contact angle models.

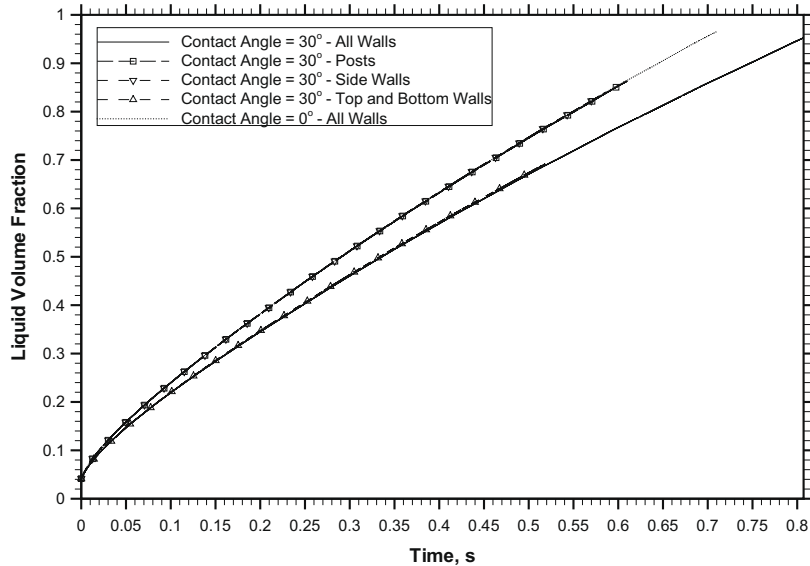


**Fig. 4.** The comparison of liquid volume fraction vs time with ethanol for 40  $\mu\text{m}$  microchannel. Contact angle of  $30^\circ$  is independently applied on each of the walls while keeping the other walls at  $0^\circ$ .

**Fig. 5** shows the relative contribution of each of the microchannel walls on liquid volume fraction for dynamic contact angle wall boundary condition. Here the working fluid is ethanol and the height of the pillared microchannel chosen for this study is 40  $\mu\text{m}$ . The dynamic contact angle is applied independently at a given wall where as the remaining walls are maintained at static contact angle ( $0^\circ$ ). The dynamic surface adhesions contribution of top and bottom wall is observed to significantly dominate than compared to the side walls and pillars. However, the relative contribution of side walls and pillars increases for a 120  $\mu\text{m}$  high microchannel as shown in **Fig. 6**. Thus, the effect of the side walls and pillars increases with increase of the height of the microchannel.

**Fig. 7** shows the relative contribution of each of the walls on liquid volume fraction with DI water for a 120  $\mu\text{m}$  high microchannel with circular pillars when dynamic contact angle is independently applied on each of the walls while keeping the other

walls at static contact angle of  $0^\circ$ . It is found that the surface adhesion contribution of the side walls and pillars is significantly higher with DI water than compared with ethanol. The surface tension and viscosity of the working fluid are vital as observed here with the pronounced effect in case of DI water as compared to ethanol.

**Fig. 8** shows the relative contribution of each of the walls with DI water for a 120  $\mu\text{m}$  high microchannel with circular pillars when static contact angle of  $80^\circ$  is independently applied on each of the walls while keeping the other walls at  $0^\circ$ . It is found that the surface adhesion contribution of the side walls and pillars is significantly higher with  $80^\circ$  contact angle than compared with  $0^\circ$ . The effect of the side walls and pillars when contact angle boundary condition is applied is not significant when applied independently for lower values of contact angle. Whereas, their effect becomes very prominent when contact angle boundary condition is applied together for all the walls for higher values of contact angle.

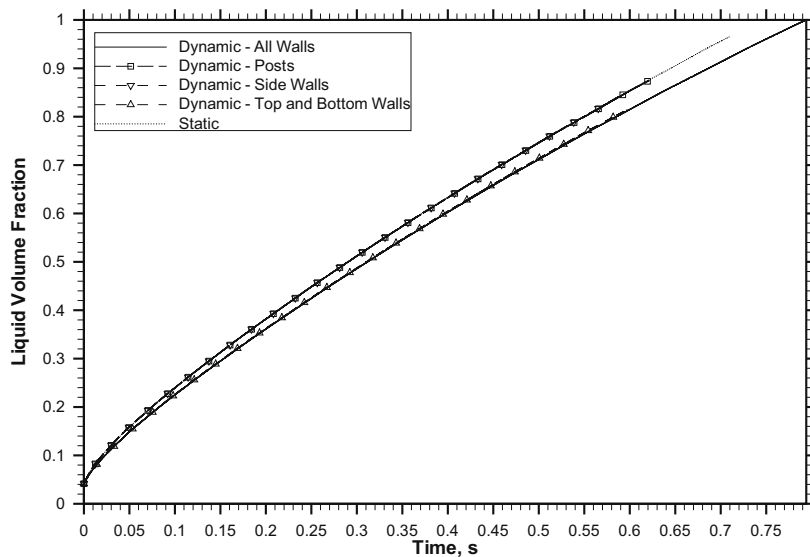


**Fig. 5.** The comparison of liquid volume fraction vs time with ethanol for 40  $\mu\text{m}$  microchannel. Dynamic contact angle is independently applied on each of the walls while keeping the other walls at static contact angle of  $0^\circ$ .

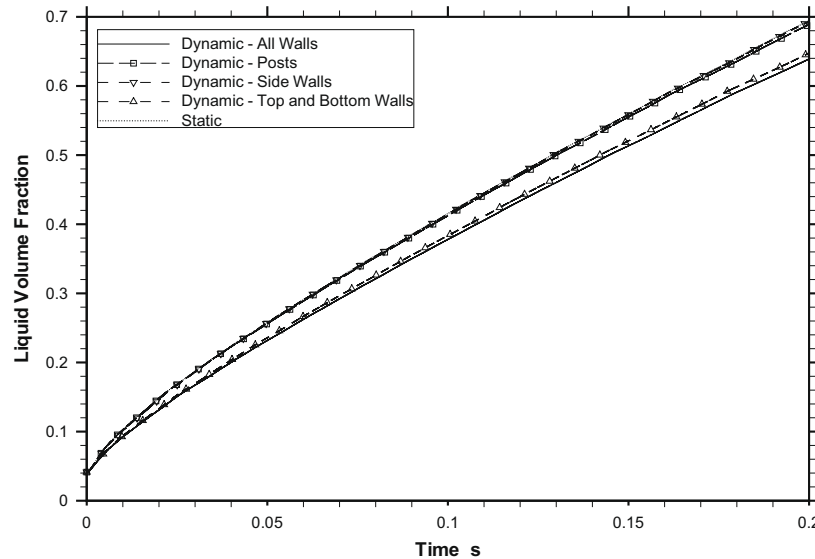


**Fig. 6.** Liquid volume fraction with ethanol for 120  $\mu\text{m}$  microchannel. Dynamic contact angle is independently applied on each of the walls while keeping the other walls at static contact angle of 0°.

### 3.1.3. Experimental verification

Saha and Mitra [1] have reported the experimental and numerical study of capillary driven flow in microchannels with integrated pillars using static contact angle approach for fully wetted wall conditions. In this paper we present the experimental results for both partially wetted and fully wetted wall conditions not yet reported and compare the results obtained earlier using static contact angle approach with the dynamic contact angle results here. The details of the fabrication of the device and experimental setup has been reported elsewhere [1].

Fig. 9 shows the variation of meniscus displacement with time for different dynamic contact angle models in a microchannel with integrated pillars (40  $\mu\text{m}$  height – PDMS substrate) with isopropyl alcohol as working fluid. It is observed that, the capillary meniscus displacement is not uniform due to the presence of pillars. The flow is faster in the converging section and slows down in the diverging section and then becomes uniform where there are no pillars. The

non uniformity in meniscus displacement due to the presence of pillars is observed to decrease with different dynamic contact angle models. It is interesting to note that, the meniscus displacement along the microchannel side wall is slightly faster compared to centerline meniscus displacement, which is shown in the bottom left inset plot in Fig. 9. Our experimental observations have also shown the above phenomena and simulated meniscus profiles show good agreement with the experimental meniscus profiles for isopropyl alcohol and the presence of pillars creates uniform meniscus front in the microchannel [1].

Fig. 10 shows the comparison of meniscus centerline velocity with time obtained numerically with experiment for pillared microchannel (120  $\mu\text{m}$  height – SU8 substrate) with ethanol as a working fluid. It was also observed during the experiments that, always a thin liquid film is formed adjacent to the meniscus interface for the working medium. Thus the interface motion is always wet due to the high wetting properties of the test liquids. Good agree-

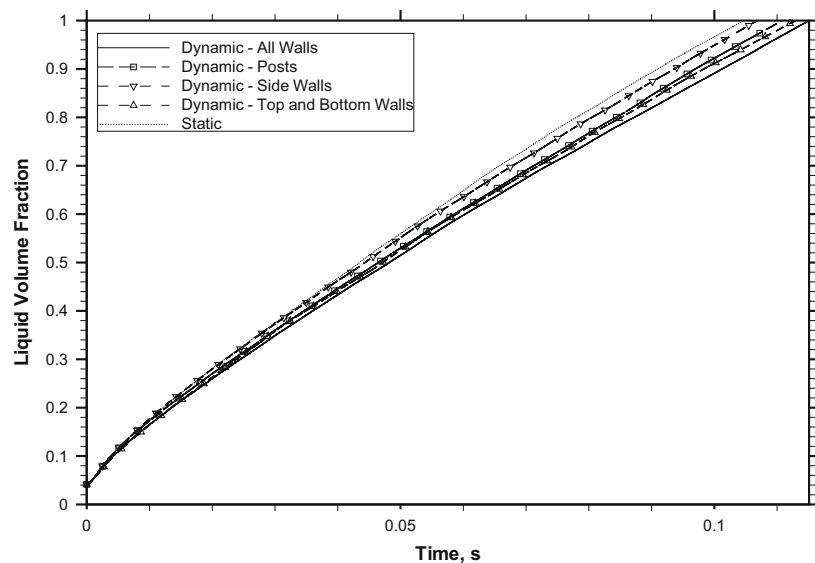


**Fig. 7.** The comparison of liquid volume fraction vs time with DI water for 120  $\mu\text{m}$  microchannel. Dynamic contact angle is independently applied on each of the walls while keeping the other walls at static contact angle of 0°.

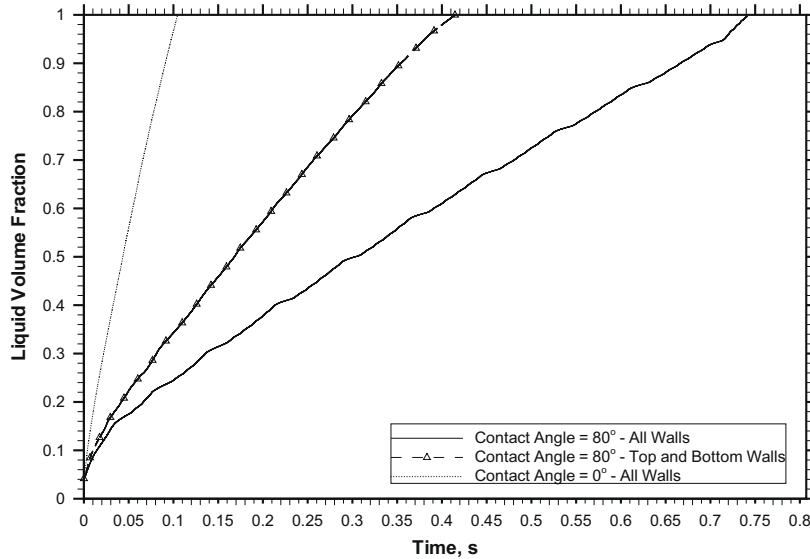


**Fig. 8.** The comparison of liquid volume fraction vs time with DI water for 120  $\mu\text{m}$  microchannel. Static contact angle of  $80^\circ$  is independently applied on each of the walls while keeping the other walls at  $0^\circ$ .

ment is found between the numerical and experimental results, except the initial starting period where the experimental results do not show good agreement. For most of the filling time, the meniscus centerline velocity is almost same under the static and dynamic contact angles. Also, the meniscus profiles are observed to have little effect using the different dynamic contact angle models as shown in the inset plot.

Figs. 11 and 12 show the comparison of the numerically obtained meniscus centerline velocity with time with those observed in experiments for SU8 pillared microchannel and DI water as a working fluid. Two cases are considered here. The first case represents when the microchannel is partially wet. It is found that the meniscus centerline velocities obtained experimentally are lower compared with the numerical results with contact angle  $0^\circ$ . This test shows that the actual contact angle in the microchannel will be very much larger than than  $0^\circ$ . We could not get enough data points due to the faster dynamics with DI water with fully wetted walls.

For the second case, experiments are conducted when the microchannel is dry. Repeated numerical simulation with different wall contact angles showed that the experimental meniscus centerline velocity of DI water in SU8 microchannel matches with the numerical simulation at wall contact angle =  $80^\circ$  (Fig. 12). It may be noted that it is often difficult to get contact angle in situ measurements due to the three dimensional geometry of the microchannel. Moreover, the sessile drop static contact angle information obtained by ex situ measurements cannot be applied, as the experimental conditions coupled with fabrication process will significantly change the surface properties of the interior of the microchannel. Therefore, fitting the experimental data with numerical results seems to be the approach that can be applied reliably here. Good agreement is found between the numerical and experimental results with a maximum relative error less than 5%, except the initial starting period where the experimental results do not show agreement. This may be due to inertia and thus

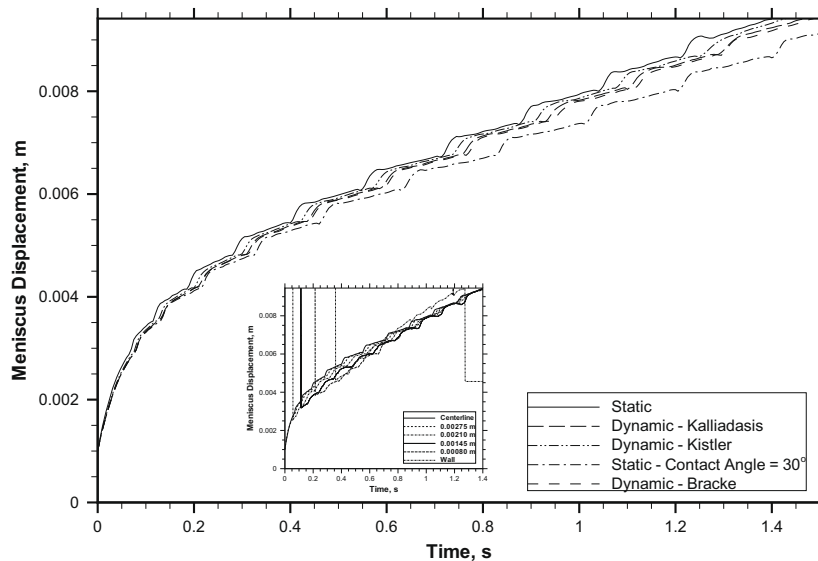


**Fig. 9.** The variation of meniscus displacement with time for different dynamic contact angle models for a pillared microchannel with isopropyl alcohol. The bottom left inset plot shows the meniscus displacement profile obtained along probe lines in the direction of flow between pillars.

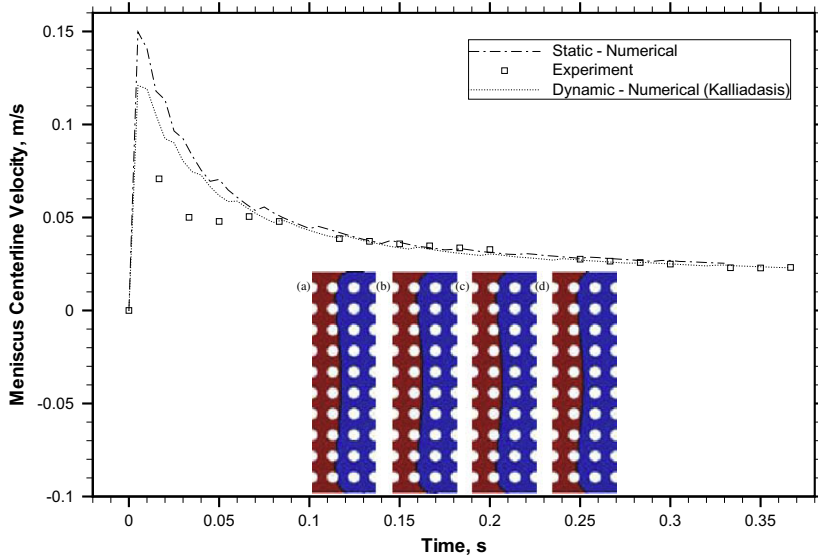


**Fig. 10.** The comparison of meniscus centerline velocity with time obtained numerically with experiment for the pillared microchannel with ethanol. The inset plot shows the meniscus profile obtained when the microchannel is half filled from different dynamic contact angle models ((a) Static, (b) Kistler, (c) Kalliadasis, (d) Bracke), where the solid black line represents the meniscus interface.

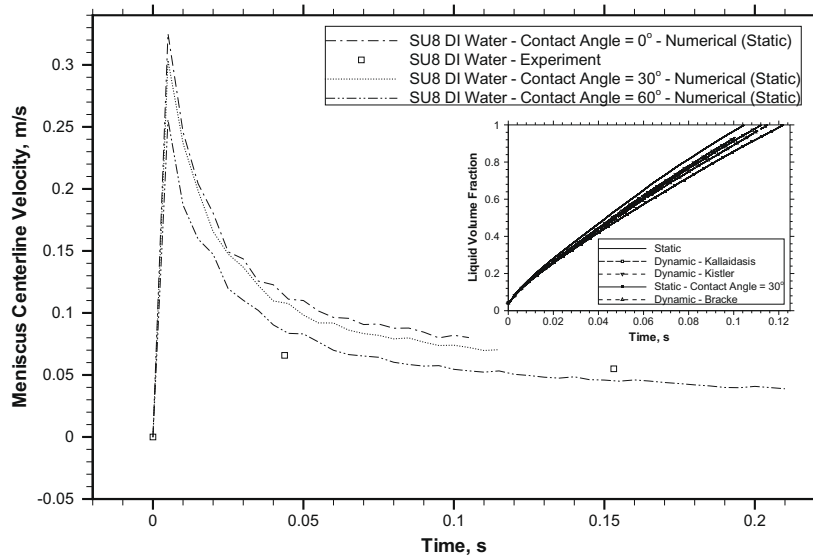
dynamic effects become important during the initial phases of the flow. The above approach has also been used by Fang et al. [32] to numerically study the three-dimensional contact angle hysteresis.

Fig. 13 shows the comparison of liquid volume fraction variation with different dynamic contact angle models for a pillared microchannel (120  $\mu\text{m}$  height) with DI water as working medium. With DI water, we have observed that, as the static contact angle increases, the difference between static and dynamic predictions of the liquid volume fraction reduces. Our numerical study indicates that, the dynamic contact angle effects are observed to be significant when the walls are fully wet (Contact angle = 0°). It is observed that the Kistler's dynamic contact angle model predicts slightly lower liquid volume fraction compared with the static contact angle model. However, Bracke's dynamic contact angle model shows substantial deviation compared with the static and Kistler's model. The top left and bottom right inset plots in Fig. 13 shows the

comparison of numerical and experimentally obtained meniscus profile with DI water and dyed DI water in the microchannel at wall contact angle = 80°. Good agreement is found between the numerical and experimental results considering static contact angle model, except the initial starting period where the experimental results do not show agreement. This may be due to slight differences in the initial condition set up in the experiments compared with numerical computations and other fabrication related issues with the microfluidic devices [1].

### 3.1.4. Simulation using different pillar geometries

We have varied the diameter to height ( $d/h$ ) and pitch to diameter ( $p/d$ ) ratio for circular pillared microchannel and studied the effect of different dynamic contact angle models on the filling time. Further, square pillars have been used instead of circular pillars and finally we have studied the effect of reducing the number of



**Fig. 11.** The comparison of meniscus centerline velocity with time obtained numerically with experiment SU8 pillared microchannel (partially wet) with DI water. The inset plot shows the liquid volume fraction variation for different dynamic contact angle models for contact angle = 0°.

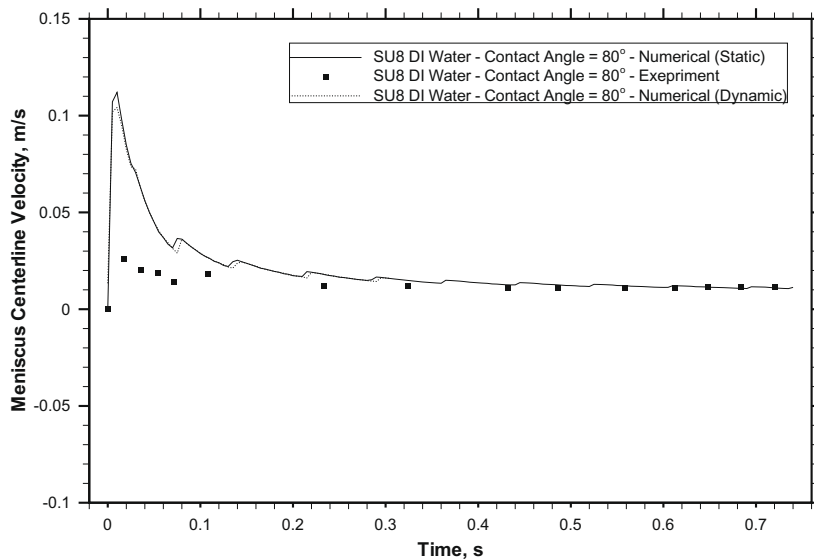


**Fig. 12.** The comparison of meniscus centerline velocity with time obtained numerically with experiment SU8 pillared microchannel with DI water.

pillars originally from 88 to 58 for both circular and square geometry. Table 2 shows the summary of the microchannel filling time for 0.9  $\mu\text{L}$  of fluid volume under different geometries. The wall contact angle is considered as  $0^\circ$  and ethanol as working medium. It is found that the dynamic contact angle models modifies the transient response of the meniscus displacement and volume of liquid filled. The observed trends are model specific and similar for all the different geometries considered in this study.

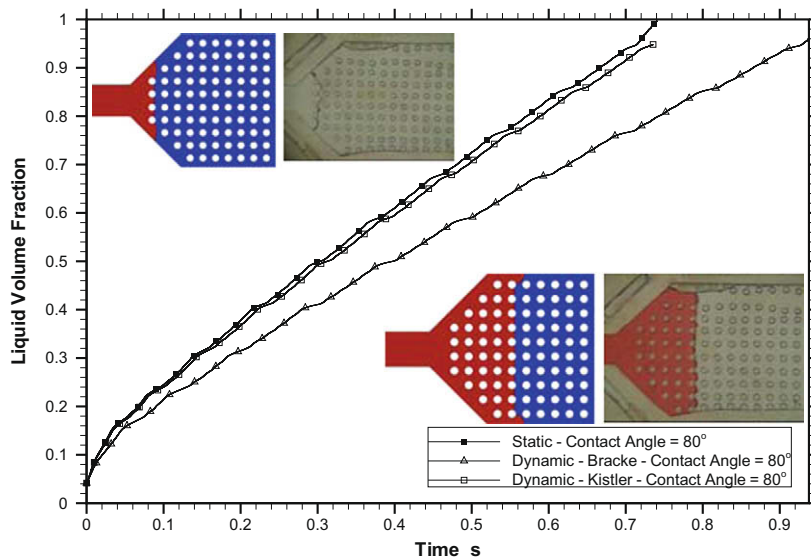
Fig. 14 shows the comparison of the profile of meniscus front at time,  $t = 0.345$  s for circular and square pillars with ethanol. The meniscus is observed to be continuous front for the circular geometry, whereas, the meniscus front is not a continuous one for the square geometry at the time instant. The liquid volume fraction variation is observed to be slightly lower for square pillars than compared with the circular pillars.

However, for larger contact angle it is found that the liquid volume fraction variation is slightly higher for square pillars than compared with the circular pillars when contact angle of  $30^\circ$  is im-

posed on the walls as shown in Fig. 15. The increase is more prominent for ethanol than compared to DI water. We infer that, the square pillar geometry is more favorable with ethanol for capillary flow than DI water.

### 3.2. Numerical accuracy and grid issues

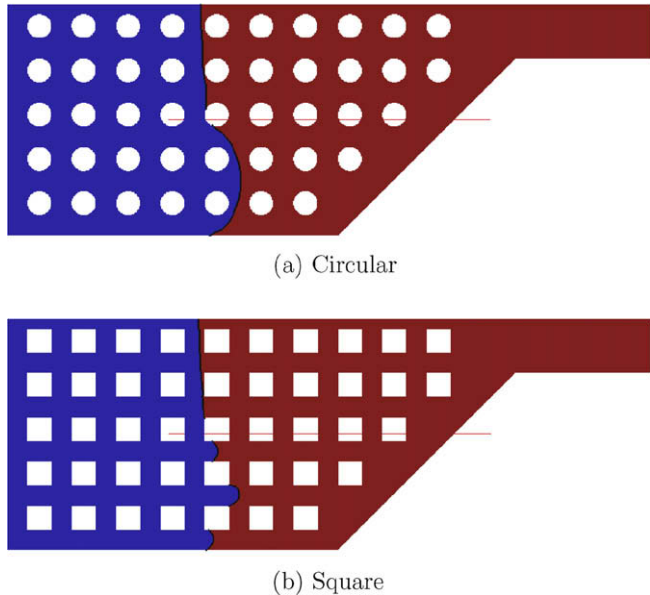
The numerical solution of free surface flow is very much dependent on the quality of the grid [33] used for the geometry of the microchannel. Grid quality depends on how the mesh is distributed in every coordinate axis direction. A  $50 \times 50 \times 10 \mu\text{m}^3$  cell size is used for generating the grid in the microchannel geometry for all the cases considered in this study. It is always necessary to keep a grid size for which the simulation time is within reasonable limits. The simulation time also depends on the dynamics of the problem, with fluid physical property (viscosity and surface tension) and the contact angle playing a vital role. The geometry of the microchannel was meshed using both structured and



**Fig. 13.** The comparison of liquid volume fraction variation with different dynamic contact angle models for the pillared microchannel with DI water. The top left and bottom right inset plot shows the profile of meniscus front with DI water and dyed DI water in the microchannel.

**Table 2**Microchannel filling time of  $0.9 \mu\text{L}$  from different geometries for ethanol.

Microchannel geometry	Contact angle model	Filling time, s
88 Round posts ( $d/h = 2.91, p/d = 1.85$ ) Total volume = $4.632 \mu\text{L}$ % Filled = 19.4	Static Kalliadasis Kistler Bracke	0.0317 0.0377 0.0362 0.0381
88 Round posts ( $d/h = 4.37, p/d = 1.85$ ) Total volume = $3.088 \mu\text{L}$ % Filled = 29.1	Static Kalliadasis Kistler Bracke	0.0819 0.0913 0.0884 0.0920
88 Round posts ( $d/h = 8.75, p/d = 1.85$ ) Total volume = $1.544 \mu\text{L}$ % Filled = 58.2	Static Kalliadasis Kistler Bracke	0.3564 0.3776 0.3692 0.3817
88 Round posts ( $d/h = 8.75, p/d = 2.60$ ) Total volume = $1.765 \mu\text{L}$ % Filled = 50.9	Static Kalliadasis Kistler Bracke	0.3316 0.3519 0.3441 0.3556
88 Round posts ( $d/h = 8.75, p/d = 1.44$ ) Total volume = $1.212 \mu\text{L}$ % Filled = 74.2	Static Kalliadasis Kistler Bracke	0.4279 0.4536 0.4404 0.4578
88 Square posts ( $d/h = 8.75, p/d = 1.85$ ) Total volume = $1.452 \mu\text{L}$ % Filled = 61.9	Static Kalliadasis Kistler Bracke	0.3728 0.3958 0.3865 0.4001
58 Round posts ( $d/h = 8.75, p/d = 1.85$ ) Total volume = $1.087 \mu\text{L}$ % Filled = 82.7	Static Kalliadasis Kistler Bracke	0.3994 0.4260 0.4153 0.4298
58 Square posts ( $d/h = 8.75, p/d = 1.85$ ) Total volume = $1.027 \mu\text{L}$ % Filled = 87.5	Static Kalliadasis Kistler Bracke	0.4322 0.4622 0.4501 0.4660

**Fig. 14.** Comparison of the profile of meniscus front having circular and square pillars with ethanol. Time = 0.345 s.

unstructured grids, as shown in Fig. 16. Table 3 shows the grid parameters for the both the cases. It is to be noted that orthogonality, skewness and aspect ratio of the grid directly affects the numerical accuracy in the VOF method. The structured grid param-

eters is observed to be favorable on the above aspects. Hence the grids considered in this present study are based on structured mesh.

The numerical accuracy of computations have been checked by refining the grids in the X-, Y-, and Z-directions. To study grid independence, the simulations have been done using 200,304 ( $50 \mu\text{m} \times 50 \mu\text{m} \times 10 \mu\text{m}$ ) and 400,608 ( $50 \mu\text{m} \times 50 \mu\text{m} \times 5 \mu\text{m}$ ) grid cells with ethanol. Fig. 17, shows that the profile of the capillary meniscus when the microchannel is 40% and 70% filled, with the two different grid sizes. It is observed that the meniscus interface is resolved well for both the grid sizes. Thus the simulation results showed that the difference between 200,304 and 400,608 grid cells is minor. Considering that the computational cost increases greatly with the node number, the computational grid with  $50 \mu\text{m} \times 50 \mu\text{m} \times 10 \mu\text{m}$  size was adopted for simulation in this study [32,34,35].

To check time-step independence, 66,768 total grid cells are used and the simulations are executed for three time steps – 0.1, 0.15 and 0.25 CFL automatic time step (ats). In Fig. 18, it is shown that the results are time-step independent with 0.1 CFL automatic time step.

The grid convergence of the solution has been tested by imposing different inlet boundary conditions viz., pressure inlet and constant velocity inlet. Similar technique is used by Saha and Mitra [3] to check grid convergence for capillary flow in a two-dimensional microchannel. We apply velocity inlet and pressure inlet boundary condition to observe the effect of grid resolution on the capillary filling time. Figs. 19 and 20 shows the variation of liquid volume fraction with time with different grid sizes for pressure and velocity inlet boundary conditions, respectively. There is no deviation in the liquid volume fraction when the grid is refined by four times

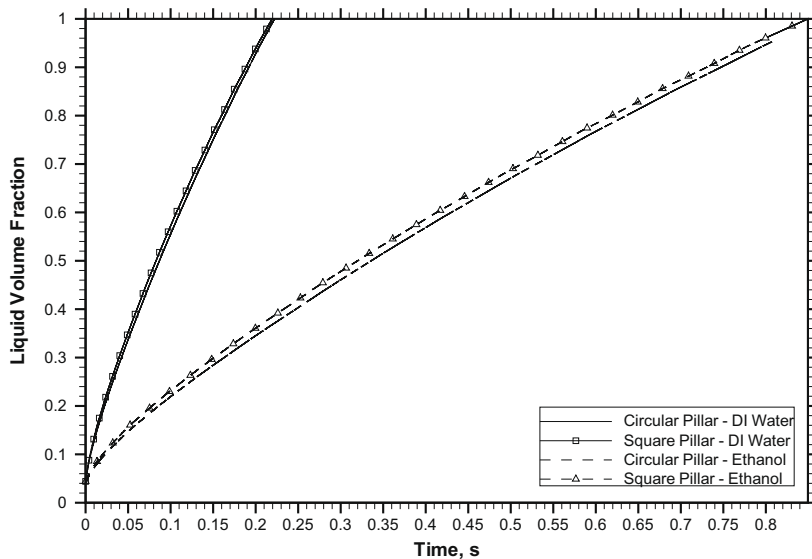
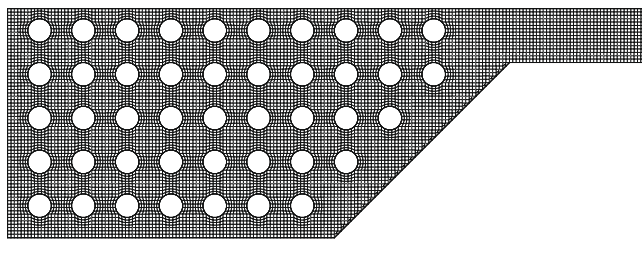
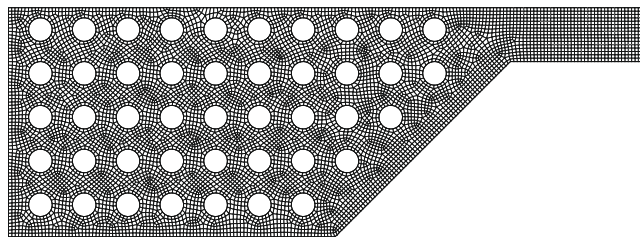


**Fig. 15.** The comparison of liquid volume fraction variation for circular and square pillars for the pillared microchannel with DI water and ethanol. Contact angle = 30°.



(a) Structured



(b) Unstructured

**Fig. 16.** Grid geometry.

only in the X-Y plane in Fig. 19. Similarly, no deviation is observed when the grid is refined by four times only in the X-Y plane and twice only in the Z-direction in Fig. 20.

However, it is found that a deviation in centerline meniscus displacement of about 2% is obtained when the grid is refined only in the Z-direction for pressure inlet boundary condition as shown in Fig. 21.

It is to be noted from that, when velocity inlet boundary conditions are imposed, the liquid volume fraction curves do not show any amount of error for all the grid sizes considered. However, when the pressure inlet boundary condition is imposed, an error of about 2% is observed in meniscus displacement as the grid is refined only in the Z-direction and there is no error as the grid is refined only in the X-Y plane. The error reduces further when a positive pressure inlet boundary condition is imposed [3]. This kind of observation is found to be in agreement also with other studies reported in literature [16,17,2,36]. The reason that the solutions

**Table 3**  
Grid parameters.

Parameters	Structured	Unstructured
Max. cell aspect ratio	5.47	7.58
Max. mesh non-orthogonality	28.71	26.53
Max. mesh skewness	0.47	0.87

give no error for velocity inlet boundary condition with grid refinement reassures the fact that the selected grid size for computation is acceptable within the numerical limitations of the algorithm.

Schonfeld et al. [16] have addressed this issue with the introduction of a macroscopic slip range in combination with a localized body force close to the contact line for the capillary rise between parallel plates. However, the approach required the usage of fitted pre-factor. On the other hand Afkhami et al. [17] have considered a mesh dependent dynamic contact angle model and showed mesh independent results for a plate withdrawal and drop spreading cases. Nevertheless, both the above studies have shown that the solution of fluid dynamic problems involving contact angles dynamics are obtained on coarse meshes itself. We intend to follow the approach of Afkhami et al. here to demonstrate the fidelity of mesh dependent dynamic contact angle model formulation for capillary filling in microchannel with integrated pillars. It may be noted that the problem considered in this present study is unique and not addressed in the above two recent articles, as we are dealing with spontaneous filling in a horizontal capillary by specifying a zero pressure at the inlet and outlet and ignoring the effect of gravity.

The mesh dependent model for applying dynamic contact angles in VOF simulations is based on the model of Cox [26] which provides a general hydrodynamic description of a moving contact line. We provide here only the expression used in the model. Interested readers may refer [17,26] for the details. The expression for the mesh dependent model is:

$$\cos \theta_{num} = \cos \theta_{app} + 5.63 \left[ \ln \left( \frac{K}{\Delta/2} \right) \right] Ca \quad (22)$$

where  $\theta_{num}$  is the mesh and velocity dependent contact angle that the interface makes with the solid surface at a distance on the order of  $\Delta/2$ ,  $\Delta$  is grid size,  $\theta_{app} = \theta_{app}(Ca, \theta_e, \dots)$  is the apparent contact angle and  $K$  is a constant. This approach of applying a boundary

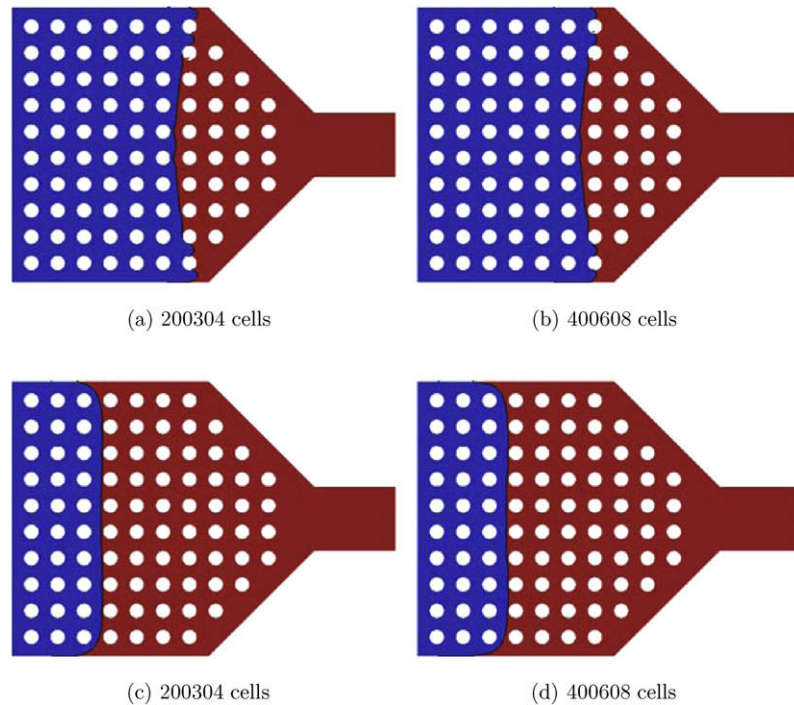


**Fig. 17.** The profile of meniscus front with ethanol in a SU8 microchannel using two different numerical grids (liquid volume fraction = 0.415532/0.41805 and 0.694201/0.694873).

condition at the contact line allows one to use mesh sizes that are very much coarser than the microscopic scale, yet obtain realistic results.

The above approach discussed allows us to implement the model without difficulty in the present VOF model as a  $\theta_d(Ca, \theta_e)$  equation. Fig. 22 shows that when the grid resolution is increased by 50% results in 1% and 0.5% error in meniscus centerline displacement with DI water for pressure inlet boundary condition with grid dependent dynamic contact angle model for  $\theta_e = 30^\circ$  and  $60^\circ$ , respectively. The error has marginally reduced with the incorporation of grid dependent dynamic contact angle model. We used  $K = 0.000002 \mu\text{m}$  in the computations. We observed that a small

value of  $K$  makes differences between  $\theta_{num}$  and  $\theta_{app}$  large. It also resulted in minimising the error. When  $K$  is selected as 2.0 for  $\theta_e = 60^\circ$  case, the predicted meniscus displacement and error slightly increased with grid refinement compared with when  $K = 0.000002$ . Large variation of  $K$  results do not appear to get affected.

The above approach is valid only when  $|\cos \theta| < 0.6$ . It may result in further reduction in error for higher values of contact angle  $\theta_e > 54^\circ$ . Initially we used a uniform value of  $\Delta$  for all the walls in our simulation, though the grid sizes are different in the spatial directions. It was observed that the error reduced slightly when using spatially different  $\Delta$  values.

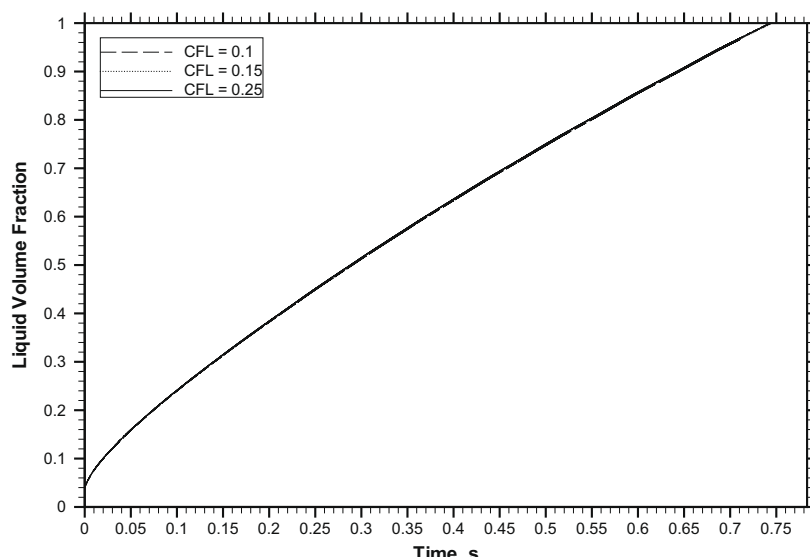


**Fig. 18.** Variation of liquid volume fraction with time with different time step sizes in a PDMS channel with ethanol.

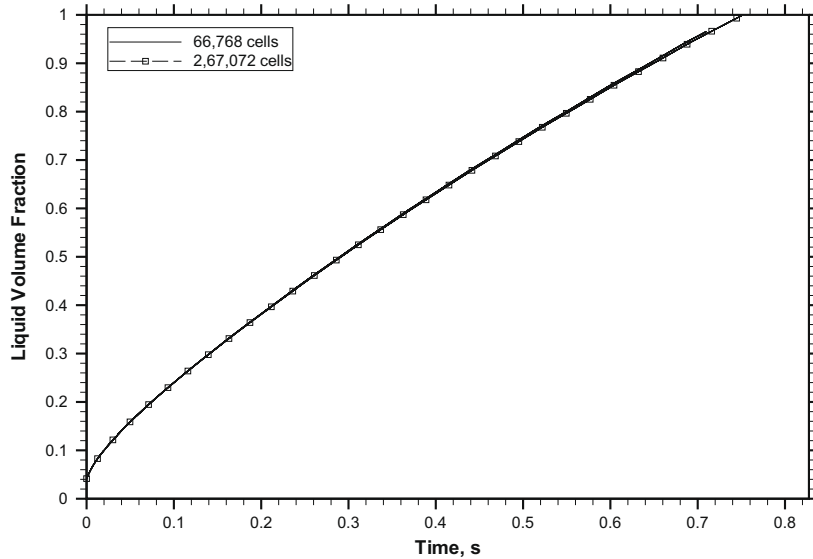


**Fig. 19.** Variation of liquid volume fraction with time with different grid sizes in a PDMS channel with ethanol for pressure inlet boundary condition.

### 3.3. Capillary phenomena considering variable surface wettability

The top and bottom wall is considered to have variable wettability characteristics having alternate patterns of hydrophilic–hydrophobic surfaces (Fig. 23). The contact angle specified on the walls of the channel is shown in Fig. 23 and summarized in Table 4. The configurations considered here are, (a) Patterned bottom wall. The cases are  $0^\circ/90^\circ$ ,  $0^\circ/60^\circ$  and  $0^\circ/30^\circ$ . A contact angle of  $0^\circ$  is specified for the top wall. (b) Patterns on both the top and bottom walls. The cases are  $0^\circ/60^\circ$ ,  $0^\circ/41.41^\circ$  and  $0^\circ/30^\circ$ .

Fig. 24 shows the plot of liquid volume fraction vs time, when the top and bottom walls having alternate hydrophilic–hydrophobic patterns with different contact angles specified. It is observed that the filling time obviously increases for the patterned configuration due to the retarding effect on the flow offered by the wall with large contact angle. However, it is found that such a patterned wall may result in better mixing of the fluid as shown in the Fig. 25, where the streamlines are observed to be non-uniform for the patterned configuration. The fluid stream is observed to cross the

adjacent pillar rows, which is not the case for a non-patterned walls (Fig. 25a). Such configurations may be suitable for biological application that require enhanced mixing. It is also noted that, a high value of contact angle specified on the walls results in the pinning of the meniscus front. It is believed that due to this pinning effect on walls, the fluid tries to take a path of least resistance thus resulting in the mixing. Also, the pinning is observed to decrease with the decrease in the wettability contrast of the patterns. The pinning is completely eliminated for a wettability contrast of  $30^\circ$  when patterns are used only on the bottom wall. The pinning effect is higher when alternate patterns are included on both the top and bottom walls compared with when the alternate patterns are specified only on the bottom wall (Fig. 25d, e and g).

Fig. 26 shows the effect of using different fluids (DI water, ethanol and isopropyl alcohol) on the liquid volume fraction, when the bottom wall having alternate hydrophilic–hydrophobic patterns with contact angles  $0^\circ/60^\circ$  and a contact angle of  $0^\circ$  for the top wall is specified. The filling time for DI water is less compared to ethanol and isopropyl alcohol. This can be attributed to the lower

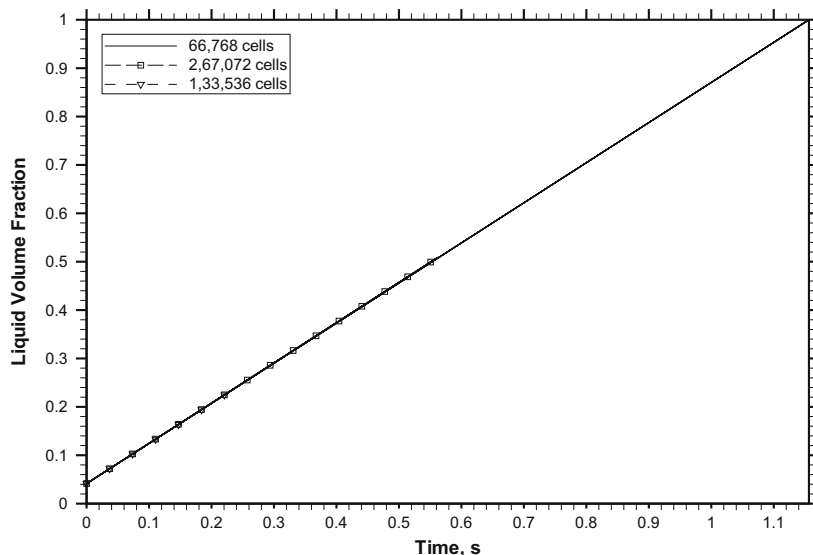


**Fig. 20.** Variation of liquid volume fraction with time with different grid sizes with ethanol for velocity inlet boundary condition.

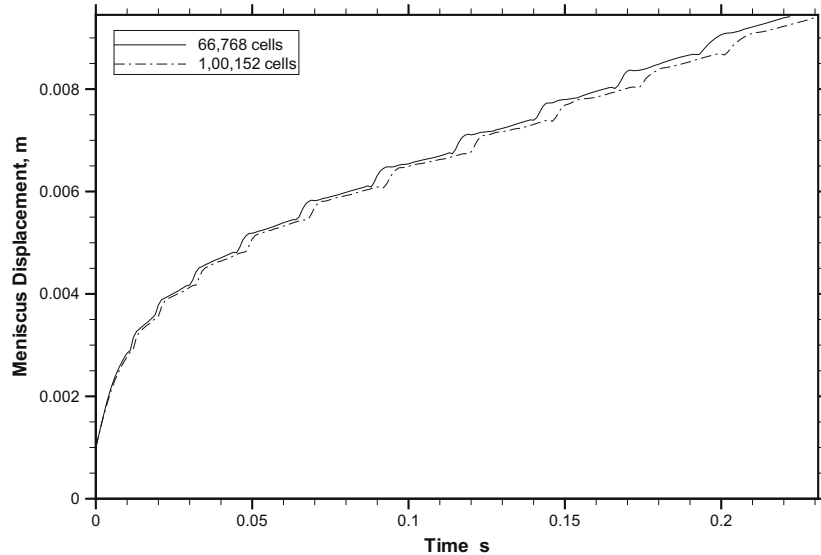


**Fig. 21.** Meniscus centerline displacement with time with different grid sizes in a PDMS channel with DI water for pressure inlet boundary condition.

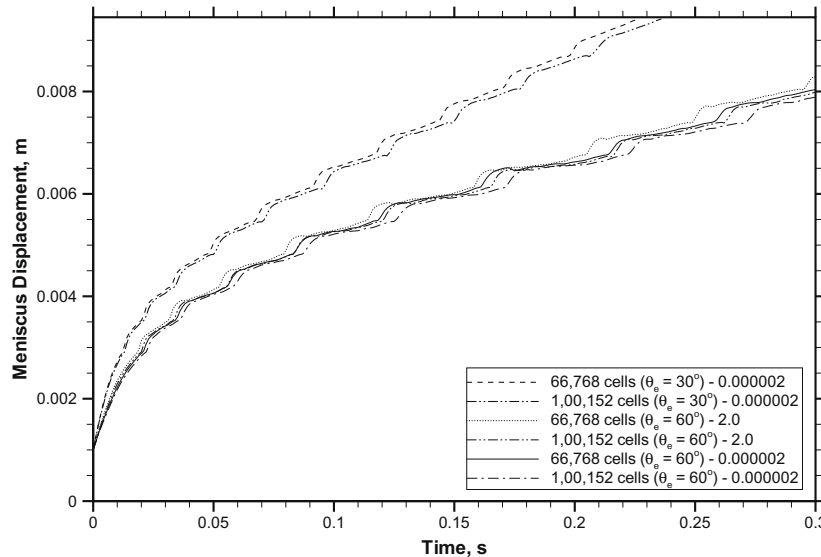
viscosity and high surface tension of DI water as compared to ethanol and isopropyl alcohol.

Fig. 27 shows the liquid volume fraction vs time, for different microchannel height with DI water when the bottom wall having alternate hydrophilic–hydrophobic patterns with contact angles  $0^\circ/60^\circ$  and a contact angle of  $0^\circ$  for the top wall is specified. The filling speed increases with increase in pillar heights.

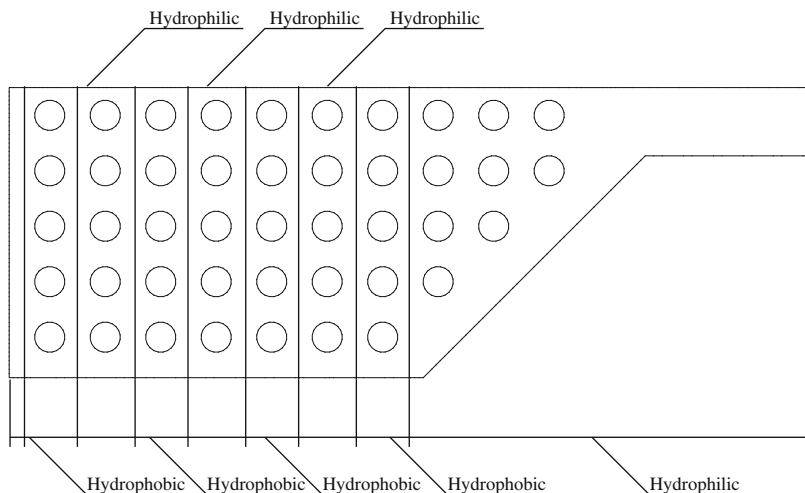
Fig. 28a and b shows the streamlines plot along with the meniscus interface obtained with ethanol and isopropyl alcohol. It is observed that for same wall contact angles specified on the bottom walls and pillar height, the pinning effect is more severe with isopropyl alcohol than compared with DI water (Fig. 25c) and ethanol. The pinning effect is found to diminish with the increase in pillar height (Fig. 25c and Fig. 28c and d). The streamline profiles shows fluid mixing behavior due the presence of alternate patterns on the bottom wall.

Fig. 29a and b show the plot of velocity component in the X-direction along the microchannel length and width, when the bottom wall having  $0^\circ/60^\circ$  alternate hydrophilic–hydrophobic

patterns with different pillar height and working medium. The hydrophilic and hydrophobic regions have been marked in the plot. It is observed that, the velocity of the meniscus increases/decreases when the flow reaches the hydrophilic/hydrophobic interface region on the bottom wall. Whereas, for a non-patterned wall the velocity magnitude decreases in the flow direction. It is therefore possible to manipulate fluid flow by controlling the size of the patterned surface. The velocity is observed to be higher for long pillars. Moreover the velocity obtained with DI water is much higher than ethanol and isopropyl alcohol. Such phenomena will find applications for performing biological reactions in microfluidic devices using the capillary flow. All biological reactions need sufficient incubation time to complete the reaction. It is believed that sufficient incubation time necessary for reaction to proceed will be inherently available in the patterned microchannel. The biological fluid will come in contact with surface, which will alternately assist and retard its flow. The region where the flow is retarded can be used for the reaction zone.



**Fig. 22.** Meniscus centerline displacement with time with different grid sizes with DI water for pressure inlet boundary condition with grid dependent dynamic contact angle model.



**Fig. 23.** Arrangement of alternate hydrophilic–hydrophobic patterns in a pillared microchannel.

**Table 4**  
Different wall configurations.

Case	Contact angle boundary condition	
	Bottom wall	Top wall
1	$\theta_1 = 0^\circ, \theta_2 = 90^\circ$	$\theta_1 = 0^\circ, \theta_2 = 0^\circ$
2	$\theta_1 = 0^\circ, \theta_2 = 60^\circ$	$\theta_1 = 0^\circ, \theta_2 = 0^\circ$
3	$\theta_1 = 0^\circ, \theta_2 = 60^\circ$	$\theta_1 = 0^\circ, \theta_2 = 60^\circ$
4	$\theta_1 = 0^\circ, \theta_2 = 41.41^\circ$	$\theta_1 = 0^\circ, \theta_2 = 41.41^\circ$
5	$\theta_1 = 0^\circ, \theta_2 = 30^\circ$	$\theta_1 = 0^\circ, \theta_2 = 0^\circ$
6	$\theta_1 = 0^\circ, \theta_2 = 30^\circ$	$\theta_1 = 0^\circ, \theta_2 = 30^\circ$

**Fig. 30** shows the meniscus displacement for four cases with DI water ( $0^\circ/60^\circ - 80\mu\text{m}, 0^\circ/30^\circ - 40\mu\text{m}, 0^\circ/60^\circ - 60\mu\text{m}$ ) that do not exhibit pinning of the meniscus front when the bottom wall having alternate hydrophilic–hydrophobic patterns is specified. The hydrophilic–hydrophobic regions are marked that shows the exact meniscus displacement profiles in the pattern regions. Meniscus displacement for a non patterned microchannel with contact angle  $30^\circ$  and height  $40\mu\text{m}$  is also plotted for comparison. **Table 5** shows the residence time of the fluid in the patterned walls obtained with DI water when the bottom wall is having different alternate hydro-

philic–hydrophobic patterns and height of microchannel. The residence time for a non patterned microchannel with contact angle  $30^\circ$  is also shown for comparison. The residence time for non patterned microchannel observed to remain same in the straight length section of the microchannel. The residence time obtained with patterned walls vary with wetting contrast of pattern and height of the microchannel. Such phenomena will find applications for performing biological reactions in microfluidic devices using the capillary flow. Using such patterned microchannel, it is possible to optimize fluid flow in microfluidic devices by manipulating the fluid residence time.

#### 4. Conclusions

It is found that the application of dynamic contact angle models had very minor effect on the capillary flow in microchannel with integrated pillars. This was verified numerically and experimentally by considering various microchannel geometries and working fluids. The study has shown that, the use of static contact angle approach seems to be adequate when using free surface VOF algorithm for microfluidic applications. The contribution of each the

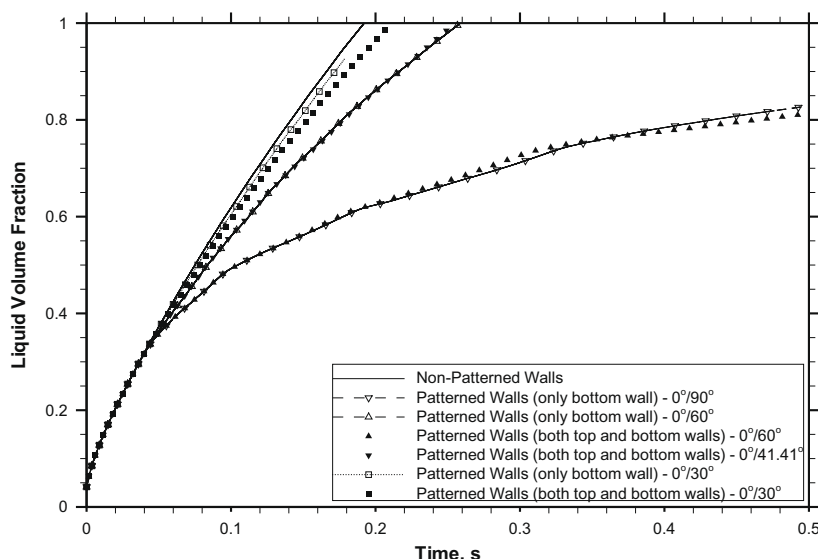


**Fig. 24.** Liquid volume fraction vs time, when the bottom wall having alternate hydrophilic–hydrophobic patterns with different contact angles is specified.

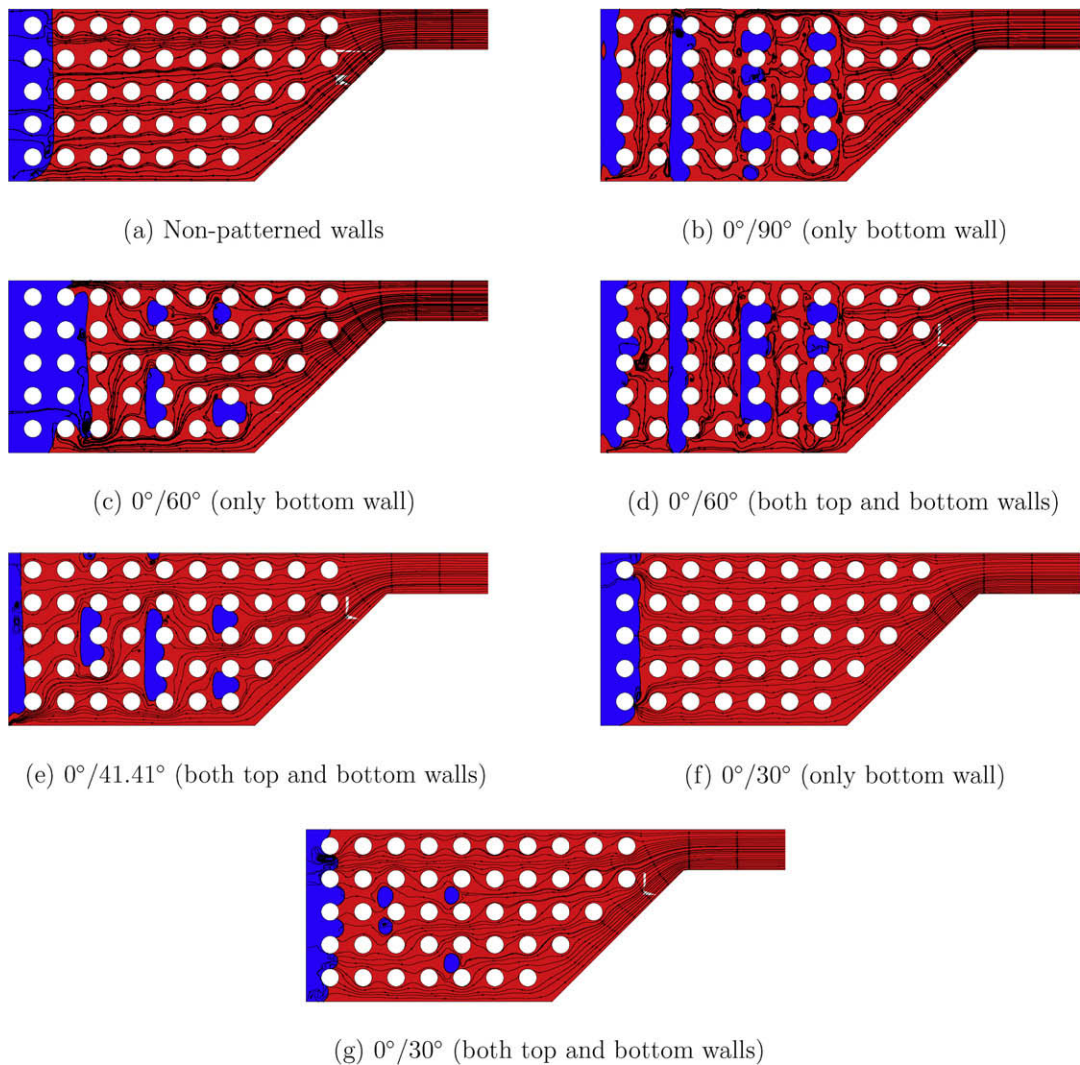


**Fig. 25.** Streamlines and meniscus interface for the patterned configuration.

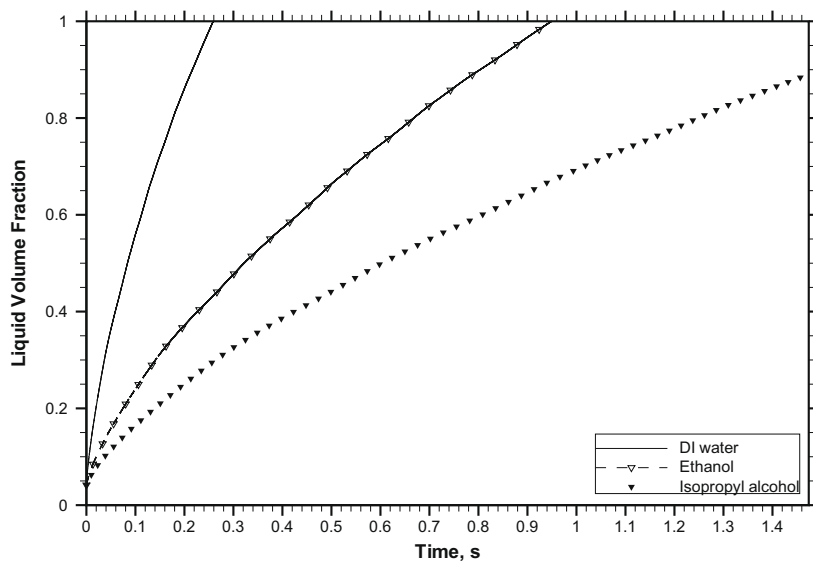


**Fig. 26.** Liquid volume fraction vs time, with the bottom wall having alternate hydrophilic–hydrophobic patterns for different working fluids.

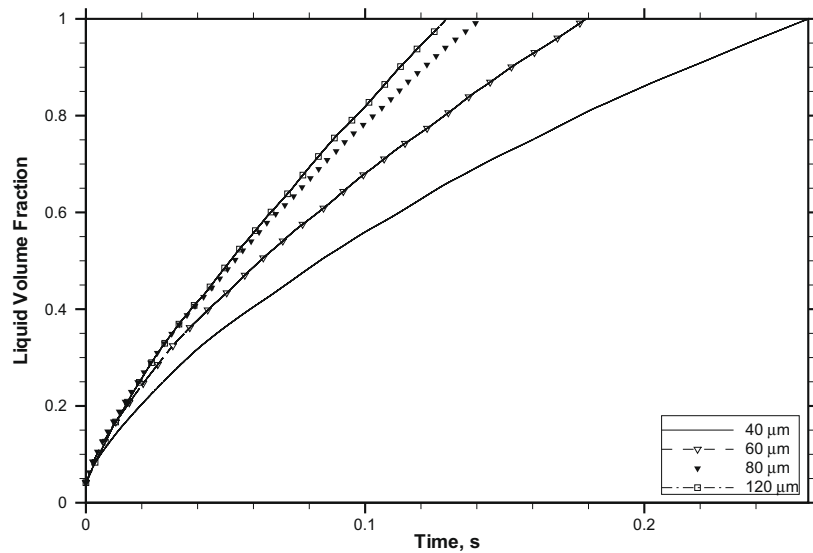


**Fig. 27.** Liquid volume fraction vs time, when the bottom wall having alternate hydrophilic–hydrophobic patterns with different pillar height.

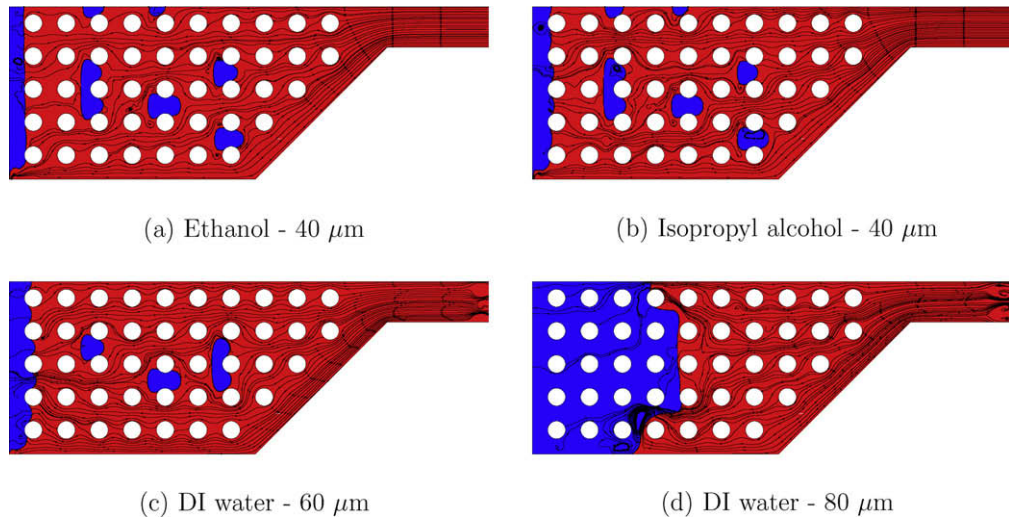


**Fig. 28.** Streamlines and meniscus interface for the patterned configuration with different fluids and microchannel height.

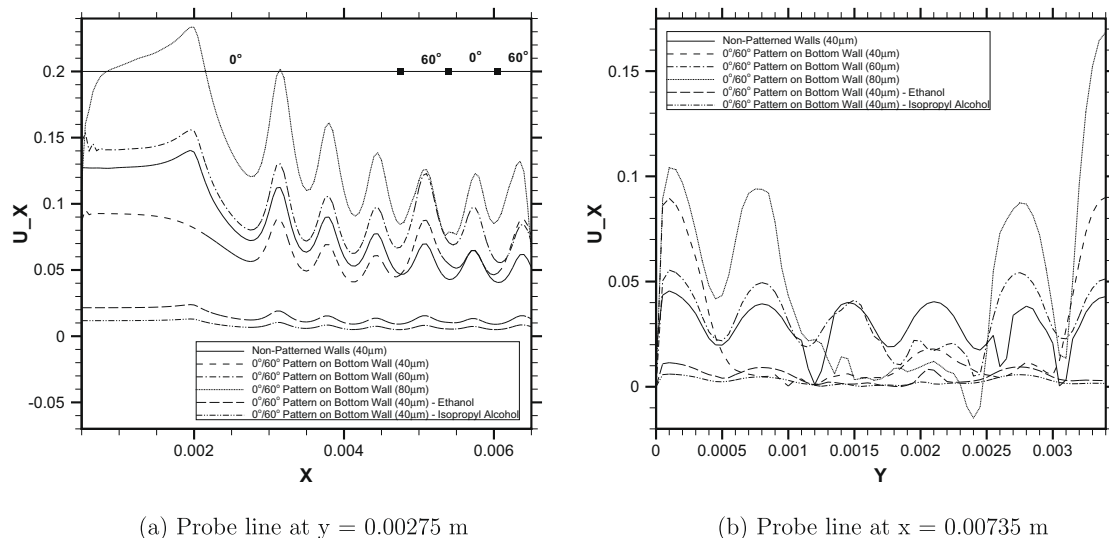


**Fig. 29.** Velocity component in the X-direction along the microchannel length and width, when the bottom wall having alternate hydrophilic–hydrophobic patterns with different contact angles is specified.

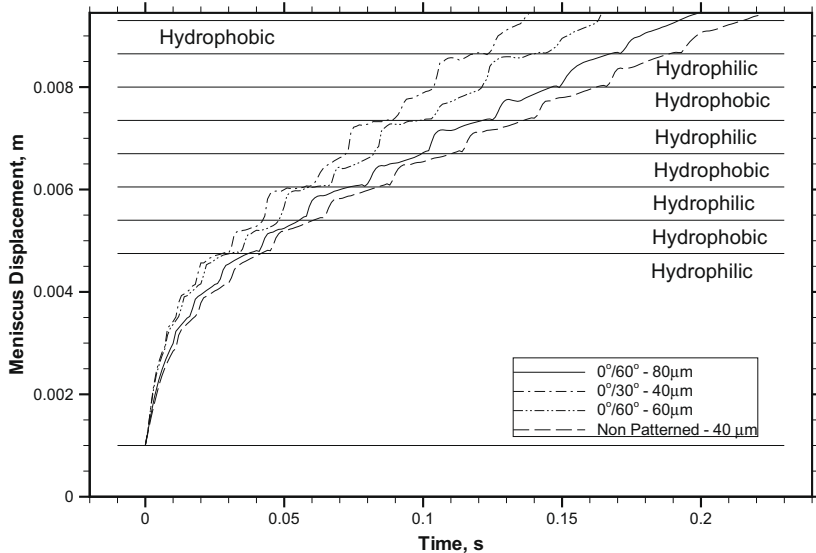


**Fig. 30.** Meniscus displacement with DI water when the bottom wall is having alternate hydrophilic–hydrophobic patterns.

**Table 5**

Residence time of the fluid in the patterned walls, ms.

Pattern	0°/60° 80 μm	0°/30° 40 μm	0°/60° 60 μm	30° Non patterned 40 μm
Hydrophilic	37.00	27.67	30.39	41.61
Hydrophobic	18.39	14.57	17.66	18.90
Hydrophilic	18.03	14.96	13.04	23.27
Hydrophobic	25.99	14.97	21.07	26.38
Hydrophilic	21.82	14.68	16.67	26.02
Hydrophobic	24.92	16.73	22.27	26.13
Hydrophilic	21.11	14.61	18.90	26.28
Hydrophobic	24.93	17.84	22.98	26.53

walls of the microchannel on the surface adhesion force was emphasized. The effect of side walls and pillars becomes very prominent when contact angle boundary condition is applied together for all the walls for higher values of contact angle than compared to smaller values of contact angle. Different inlet boundary conditions has been imposed to observe the effect of grid resolution and a grid dependent dynamic contact angle model has been applied to demonstrate grid independence for the spontaneous/passive capillary flow. The grid independence was shown to improve marginally by applying the grid dependent dynamic contact angle model. Capillary phenomena considering variable surface wettability with alternate hydrophilic–hydrophobic patterns on top and bottom walls has been studied for the microchannel with integrated pillars. Non-uniform streamlines was observed to be formed when using patterned walls. The meniscus front pinning was noticed for a high wetting contrast between the patterns. The pinning of the meniscus front can be eliminated with the increase in the height of the microchannel and reducing the wetting contrast between the patterns. Such configurations may find applications in the area of biological sampling and detection that require enhanced mixing.

## References

- [1] A.A. Saha, S.K. Mitra, M. Tweedie, S. Roy, J. McLaughlin, Microfluid. Nanofluid. (2008), doi:10.1007/s10404-008-0395-0.
- [2] W. Huang, Q. Liu, Y. Li, Chem. Eng. Technol. 26 (2006) 716–723.
- [3] A.A. Saha, S.K. Mitra, J. Fluids Eng. 131 (2009) 061202-1–061202-12.
- [4] A.A. Saha, S.K. Mitra, Investigation of three-dimensional flow in microchannels with patterned surfaces, in: 5th International Conference on Nanochannels, Microchannels and Minichannels, Puebla, Mexico, 2007, pp. 1–8, paper No. 30052.
- [5] C.W. Hirt, B.D. Nichols, J. Comput. Phys. 39 (1981) 201–225.
- [6] R. Scardovelli, S. Zaleski, Annu. Rev. Fluid Mech. 31 (2008) 567–603.
- [7] L. Grader, Colloid Polym. Sci. 264 (1986) 719–726.
- [8] M.N. Popescu, J. Ralston, R. Sedev, Langmuir 24 (2009) 12710–12716.
- [9] T.D. Blake, J. Colloid Interface Sci. 299 (2006) 1–13.
- [10] X. Wang, X. Peng, B. Wang, Heat Transfer – Asian Res. 35 (2006) 1–12.
- [11] C.W. Hirt, J.M. Brethour, Moving contact lines on rough surfaces, in: In 4th European Coating Symposium, 2001, FloSci-Bib17-01.
- [12] G. Rosengarten, D.J.E. Harvie, J.C. White, Appl. Math. Modell. 30 (2006) 1033–1042.
- [13] R.L. Hoffman, J. Colloid Interface Sci. 75 (1975) 228–241.
- [14] J. Ralston, M. Popescu, R. Sedev, Annu. Rev. Mater. Res. 38 (2008) 23–43.
- [15] M. Renardy, Y. Renardy, J. Li, J. Comput. Phys. 171 (2001) 263–343.
- [16] F. Schonfeld, S. Hardt, Comput. Fluids 38 (2009) 757–764.
- [17] S. Afkhami, S. Zaleski, M. Bussmann, J. Comput. Phys. (2009), doi:10.1016/j.jcp.2009.04.027.
- [18] J.U. Brackbill, D.B. Kothe, C. Zemach, J. Comput. Phys. 100 (1992) 335–354.
- [19] J. Zeng, On modeling of capillary filling, <[http://www.coventor.com/pdfs/on\\_modeling\\_of\\_capillary\\_filling.pdf](http://www.coventor.com/pdfs/on_modeling_of_capillary_filling.pdf)>, 2007 (accessed 15.03.07).
- [20] T.S. Jiang, S.G. Oh, J.C. Slattery, J. Colloid Interface Sci. 69 (1979) 74–77.
- [21] Y.D. Shikhmurzaev, Capillary Flows with Forming Interfaces, Chapman & Hall/CRC, Boca Raton, 2008.
- [22] S. Kalliadasis, H.C. Chang, Phys. Fluids 6 (1993) 12–23.
- [23] S. Chakraborty, Lab Chip 5 (2005) 421–430.
- [24] S. Sikalo, H.D. Wilhelm, I.V. Roisman, S. Jakirlic, C. Tropea, Phys. Fluids 17 (2005) 062103-1–062103-13.
- [25] N. Fries, M. Dreyer, J. Colloid Interface Sci. 327 (2008) 125–128.
- [26] R.G. Cox, J. Fluid Mech. 168 (1986) 169–194.
- [27] S. Newman, J. Colloid Interface Sci. 26 (1968) 209–213.
- [28] Y. Xiao, F. Yang, R. Pitchumani, J. Colloid Interface Sci. 298 (2006) 880–888.
- [29] OpenCFD Ltd., OpenFOAM User Guide, Version 1.5 Edition, 2008.
- [30] O. Ubbink, R.I. Issa, J. Comput. Phys. 153 (1999) 26–50.
- [31] H. Rusche, Computational fluid dynamics of dispersed two-phase flows at high phase fractions, Ph.D. Thesis, Imperial College, University of London, London, 2002.
- [32] C. Fang, C. Hidrovo, F.M. Wang, J. Eaton, K. Goodson, Int. J. Multiphase Flow 34 (2008) 690–705.
- [33] J.A. Sethian, P. Smereka, Ann. Rev. Fluid Mech. 35 (2003) 341–372.
- [34] A.S. Yang, Int. J. Mech. Sci. 50 (2008) 1304–1315.
- [35] Y.F. Chen, F.G. Tseng, S.Y.C. Chien, M.H. Chen, R.J. Yu, C.C. Chieng, Microfluid. Nanofluid. 5 (2008) 193–203.
- [36] W. Huang, personal communication.